# A fully coupled hydro-mechanical model for the modeling of coalbed methane recovery

François BERTRAND[a,b,c,*], Benjamin CERFONTAINE[a], Frédéric COLLIN[a]

[a] *University of Liege, Urban and Environmental Engineering / Geomechanics, 4000 Liege, Belgium*
[b] *University of Newcastle, Priority Research Centre for Geotechnical and Materials Modeling, Callaghan, NSW 2308, Australia*
[c] *F.R.I.A, Fonds de la Recherche Scientifique - FNRS, 1000 Brussels, Belgium*

**Abstract**

Most coal seams hold important quantities of methane which is recognized as a valuable energy resource. Coal reservoir is considered not conventional because methane is held adsorbed on the coal surface. Coal is naturally fractured, it is a dual-porosity system made of matrix blocks and cleats (i.e fractures). In general, cleats are initially water saturated with the hydrostatic pressure maintaining the gas adsorbed in the coal matrix. Production of coalbed methane (CBM) first requires the mobilization of water in the cleats to reduce the reservoir pressure. Changes of coal properties during methane production are a critical issue in coalbed methane recovery. Indeed, any change of the cleat network will likely translate into modifications of the reservoir permeability.

This work consists in the formulation of a consistent hydro-mechanical model for the CBM production modeling. Due to the particular structure of coal, the model is based on a dual-continuum approach to enrich the macroscale with microscale considerations. Shape factors are employed to take into account the geometry of the matrix blocks in the mass exchange between matrix and fractures. The hydro-mechanical model is fully coupled. For example, it captures the sorption-induced volumetric strain or the dependence of permeability on fracture aperture, which evolves with the stress state. The model is implemented in the finite element code Lagamine and is used for the modeling of one production well. A synthetic reservoir and then a real production case are considered. To date, attention has focused on a series of parametric analyses that can highlight the influence of the production scenario or key parameters related to the reservoir.

*Keywords:* Coalbed methane, Dual-porosity, Shape factor, Couplings, Reservoir modeling

## 1. Introduction

Coal seams typically contain large amounts of methane which can be recovered in the form of natural gas, the so-called coalbed methane (CBM) [1]. This methane is mainly located in Russia, Canada, China, Australia, and the USA. The first recorded well was drilled in 1931 in the USA in West Virginia but the commercial exploitation really began in the 1980s. The three major basins are the Black Warrior Basin (Alabama), the San Juan Basin (New Mexico, Utah, Colorado) and the Powder River basin (Wyoming and Montana) [2]. Thanks to these basins, the USA is currently the largest CBM producer in the world. About 90,000 CBM wells have been drilled in the USA, producing annually between 1 and 2 trillion cubic feet in the recent years (Figure 1). It represents almost 10% of the American natural gas production [3]. CBM production decreased in the past years but it is likely correlated to the oil price because American basins are expected to produce significant amounts of methane for at least one or two decades [4].

In order to determine the best production scenario, numerical models are interesting tools for oil and gas companies. However, models developed for conventional reservoirs are not suitable for the modeling of the CBM production. In conventional models, hydrocarbons are stored in porous and permeable host rocks with free gas compressed into the pore space (Figure 2a). In this case, gas flow rate is almost at the highest level from the beginning and it gradually declines accompanied by the increase of the water production (Figure 3a). In coal reservoirs, there are actually two key parts constituting the porosity system, fractures and much smaller pores in the matrix [4]. Methane is mainly stored by adsorption in the coal matrix while fractures,

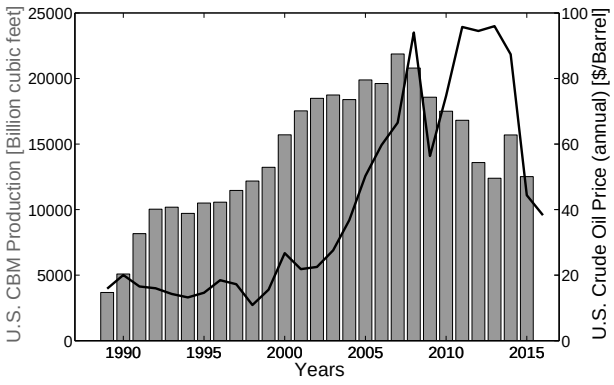


Figure 1: CBM estimated production in the USA compared with oil price. *Data from the U.S. Energy Information Administration.*

*Francois.Bertrad@ulg.ac.be

termed cleats [5], contain minor amounts of free gas (Figure 2b). Thanks to sorption, coal can contain per unit volume six to seven times more gas than sandstone from a conventional reservoir [6]. The maximum amount of sorbed gas non linearly increases with the reservoir pressure (Figure 4). It is the hydrostatic pressure that generally maintains the gas adsorbed in the coal matrix. Cleats are water saturated and production of CBM first requires the mobilization of water to reduce the reservoir pressure. This reduction of pressure in the coal seam is followed by desorption of methane from the matrix. Gas molecules then diffuse through the matrix, migrate through the cleat system, and finally reach the wellbore or the mine shaft (Figure 5) [7]. The typical gas and water production profiles are therefore not surprisingly distinct from a conventional reservoir. In the case of coal reservoir, gas rate peaks after water and the rising production can last from a few months up to years. As a result, the peak gas rate can be observed up to few years after the start of the production [8].

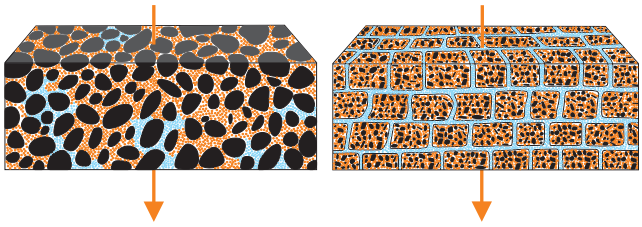


Figure 2: Comparison of gas storage in conventional reservoirs (a) and coalbed (b). Gas in orange, water in blue and solid grains in black. *Modified from* [2].

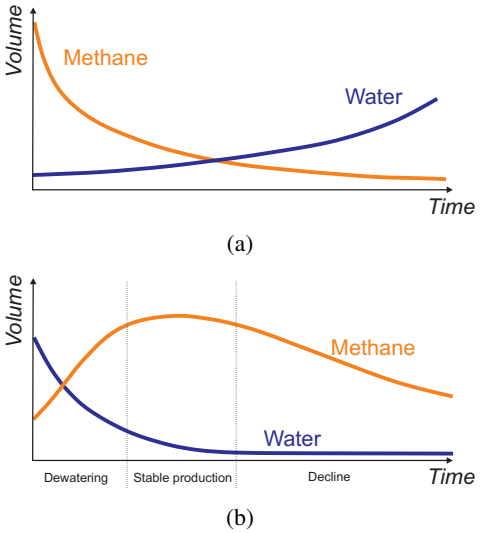


Figure 3: Comparison of gas and water production profiles from conventional reservoirs (a) and coalbed (b). *Modified from* [2].

Due to the coal structure, transport mechanisms through coalbed are dual: flows are diffusive in the coal matrix and advective in the cleats [9, 10]. Cleats aperture is therefore an important characteristic of the reservoir. Any change of the cleat network modifies the reservoir permeability. In particular, two distinct phenomena are known to result from reservoir

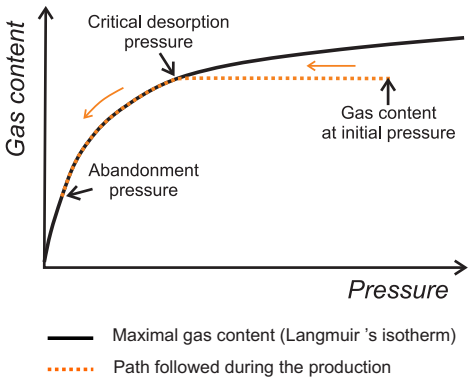


Figure 4: Relation between the gas content and the reservoir pressure. *Modified from* [2].

pressure depletion, which have opposite effects on coal permeability [11]:

- The first phenomenon is the reservoir compaction due to the increase in the effective stress after the reservoir depletion. It tends to decrease the permeability.
- The second is the matrix shrinkage following the gas desorption from the coal. It increases the cleat permeability.

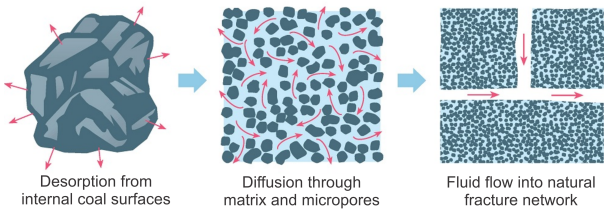


Figure 5: Gas migration in coal seams, [7].

The recovery of coalbed methane can be enhanced by a stimulation treatment as hydraulic fracturing or $CO_2$ injection. The hydraulic fracturing enhances the natural fractures network to increase the permeability while the $CO_2$ injection accelerates the kinetics of the methane desorption. Indeed, carbon dioxide has a higher affinity for coal and thus displaces methane locked within the coal matrix [12]. However, a $CO_2$ molecule placed between the polymer chains of coal partly disrupts the original structure of coal which swells [13]. Therefore, the resorption of $CO_2$ could have a detrimental impact on the permeability of the reservoir [14].

CBM production involves multi-physical aspects and it is a highly coupled problem. Moreover, coal presents a two-scale porosity system, what makes simple macroscale models particularly inappropriate to obtain the production profiles observed in Figure 3b. In many existing CBM models encountered in the literature, sorption- and stress-induced coal permeability alteration is a remarkable aspect which is improperly simplified [15]. The objective of this paper is to formulate a hydro-mechanical model able to reproduce the production curves from Figure 3b and catching the hydro-mechanical couplings influencing the permeability. In this purpose, the model is based on

a dual-continuum approach to enrich the macroscale with microscale considerations. The novelty consists in combining the use of shape factors with a permeability model directly linked to fracture aperture. On the first hand, the shape factor accounts for the diffusive processes taking part in the matrix and the gas exchange between the matrix and the cleats. On the other hand, the permeability model is used for advective multiphase flows in the fractures. It is not usual in the literature to link the permeability evolution with the fracture aperture evolution, it is generally linked to the porosity evolution. In this paper, the cleat aperture evolves with the desorption rate and the stress state, what requires the employment of a dual-continuum approach for both the mechanical and the hydraulic parts of the model. The model is developed for a single gas species, enhanced coalbed methane modeling is therefore out of the scope of this paper.

In the following, the general framework for the modeling of geomaterials is first introduced. Then, the mechanical and hydraulic laws are presented before considering the hydro-mechanical couplings taken into account to constitute the final hydro-mechanical model implemented in a finite element code (Lagamine [16, 17]). This model is finally used for the modeling of a CBM reservoir at the scale of one production well. The influences of the production scenario and the hydro-mechanical couplings on the production profiles and the permeability evolution are highlighted. A history matching exercise is also performed with data obtained from a well drilled in the Horseshoe Canyon coals (Canada).

## 2. General framework for geomaterials

### 2.1. Porous medium

The structure of geomaterials is complex, it is an assembly of solid grains forming a solid skeleton and fluids can fill the porous space between these grains (Figure 6). The full description of this system is almost impossible. For this reason, relying on a mixture theory, the real discontinuous porous medium may be modelled by superimposed continua [18].

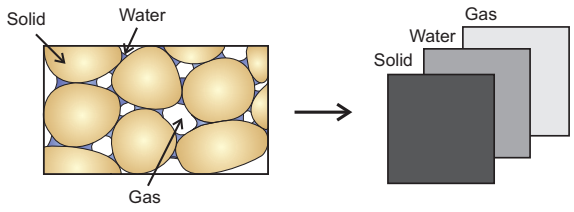


Figure 6: Porous medium and superimposed continua.

The concept of volume fractions is used to create some homogenized continua of reduced densities, allowing the application of continuum mechanics. Indeed, every point of the idealized system consists of a mixture of phases because all phases are assumed to occupy the same region of space simultaneously. The volume fraction $\eta_\pi$ of the phase $\pi$ is defined as

$$\eta_\pi = \frac{\Omega_\pi}{\Omega} \tag{1}$$

where $\Omega_\pi$ is the volume of the phase $\pi$ and $\Omega$ is the total volume of the control space. The sum of the different volume fractions of all phases is 1. The following volume fractions are defined

$$\eta_s = 1 - \phi \tag{2}$$

$$\eta_l = S_r\, \phi \tag{3}$$

$$\eta_g = (1 - S_r)\, \phi \tag{4}$$

where $s$, $l$ and $g$ denote the solid, the liquid and the gas phases respectively, $\phi$ is the total porosity defined as the ratio between the total void volume $\Omega_v$ and the total volume $\Omega$

$$\phi = \frac{\Omega_v}{\Omega} = \frac{\Omega_l + \Omega_g}{\Omega_s + \Omega_l + \Omega_g} \quad \in [0,1] \tag{5}$$

and $S_r$ is the saturation degree of the liquid phase, defined as the ratio between the volume of the liquid phase $\Omega_l$ and the porous volume $\Omega_v$

$$S_r = \frac{\Omega_l}{\Omega_v} \tag{6}$$

### 2.2. Balance equations

The balance equations of the hydro-mechanical problem consist of the balance of momentum of the mixture and the mass balance equations of the solid and the fluids.

#### 2.2.1. Momentum balance equation

For quasi-static loading and neglecting gravity, the balance of momentum of the mixture reads:

$$\frac{\partial \sigma_{ij}}{\partial x_j} = 0 \tag{7}$$

This equation introduces the total stress tensor $\sigma_{ij}$ which is related to the strains through the mechanical constitutive model (section 3). Gravity is neglected because the thickness of the coal seam is negligible compared to the depth of the seam.

#### 2.2.2. Mass balance equations

From Reynolds transport theorem, the general mass balance equation in differential form writes:

$$\frac{\partial \Upsilon}{\partial t} + \frac{\partial \varphi_i}{\partial x_i} - Q = 0 \tag{8}$$

where $\Upsilon$ is a storage term, $Q$ is the source term and the divergence of the fluxes $\varphi_i$ expresses the difference between the input and the output fluxes of the given volume.

Mass balance equations are established following a compositional approach [19, 20, 21] which consists of balancing species rather than phases. By this way, exchange terms between the phases are cancelled out. The model is developed for a single gas species which refers therefore to methane in the case of coal seam gas recovery.

Thanks to a Lagrangian description [22], the referential follows the solid skeleton which is deforming. Inside this solid framework, the description of the fluid is Eulerian.

*Solid mass balance equation.*

As the reference system follows the solid phase, there is necessarily conservation of the solid mass, it writes:

$$\frac{\partial}{\partial t}(\rho_s(1-\phi_f)\Omega) = 0 \tag{9}$$

with $\rho_s$ the solid density and $\phi_f$ the porosity from the fractures.

*Water mass balance equation.*

As water is assumed only present in the fracture system, the following single water mass balance equation is written:

$$\underbrace{\frac{\partial}{\partial t}(\rho_w S_r \phi_f) + \frac{\partial}{\partial x_i}(\rho_w\, q_{li})}_{\text{Liquid water}} + \underbrace{\frac{\partial}{\partial t}(\rho_v(1-S_r)\phi_f) + \frac{\partial}{\partial x_i}\left(\rho_v\, q_{g_i} + (1-S_r)\, J^w_{g\,i}\right)}_{\text{Water in gas phase}} = 0 \tag{10}$$

where $\rho_w$ and $\rho_v$ are the water and water vapour densities, $q_{li}$ and $q_{g_i}$ are the liquid and gas advective flows, and $J^w_{g\,i}$ is the diffusive flow of water vapour. Terms relative to vapour are presented for the sake of generalization but it is not of major interest in the context of coalbed methane production.

*Gas mass balance equation.*

For gas, present in cleats and matrix, a dual-porosity approach is adopted [23]. This concept, introduced by Barenblatt, requires to define a pressure for both fractures and matrix. The difference in pressure between the cleats and the matrix is responsible for a mass exchange $E$ between the two systems, it is a source for one and a sink for the other. This exchange is determined using shape factors (section 4.3). The gas mass balance equations, the first equation being relative to the cleats and the second one to the matrix, are:

$$\underbrace{\frac{\partial}{\partial t}(\rho_{g,f}\,(1-S_r)\phi_f) + \frac{\partial}{\partial x_i}\left(\rho_{g,f}\, q_{g_i} + (1-S_r)\, J^g_{g\,i}\right)}_{\text{Gas phase}} + \underbrace{\frac{\partial}{\partial t}\left(\rho^d_{g,f}\, S_r \phi_f\right) + \frac{\partial}{\partial x_i}\left(\rho^d_{g,f}\, q_{li} + S_r\, J^g_{l\,i}\right)}_{\text{Dissolved gas in water phase}} = E \tag{11}$$

and

$$\frac{\partial}{\partial t}\left(\rho_{g,Ad}\right) = -E \tag{12}$$

where $\rho_{g,f}$, $\rho^d_{g,f}$ and $\rho_{g,Ad}$ are respectively the densities of the gas in the cleats, the dissolved gas in the water and the gas adsorbed on the matrix. $J^g_{g\,i}$ and $J^g_{l\,i}$ represent the diffusive flows of the gas in the gas phase and the dissolved gas in the liquid phase. Equation 11 is relative to the cleats, the first brace refers to the dry gas phase while the second one refers to the dissolved gas in water. Indeed, as gas may be dissolved in water, it is transported with the water flow and may also diffuse in water. Finally, Equation 12, relative to the matrix, indicates that rate of gas storage equals the mass transfer $E$ with the cleats. This rate is the variation of the amount of gas adsorbed within the matrix. It will be evaluated in section 4.3.

## 3. Mechanical model

Coal is an elasto-brittle geomaterial and its behaviour is essentially linear-elastic prior to yielding/failure. Coals of all ages and ranks are fragile rocks, with little mechanical strength compared to conventional reservoir rocks [6]. Coal may deform plastically [24], or perhaps viscoelastically [25], but the non-elastic behaviour of coal is not well documented and most mechanical tests, especially under low strain conditions, have registered elastic behaviour [26]. An elastic constitutive law is therefore assumed effective for describing the stress-strain relationship of coal before failure. The elastic constitutive model relates stress and strain increments through the elastic stiffness tensor $C_{ijkl}$ or inversely with the elastic compliance $D_{ijkl}$:

$$\tilde{\sigma}_{ij} = C_{ijkl}\,\dot{\varepsilon}_{kl} \quad \Leftrightarrow \quad \dot{\varepsilon}_{ij} = D_{ijkl}\,\tilde{\sigma}_{kl} \tag{13}$$

where $\dot{\varepsilon}_{ij}$ is the Cauchy strain rate and $\tilde{\sigma}_{ij}$ is the Jaumann stress rate. As will be seen in section 5.1.1, it is actually an effective stress rate.

For modeling purpose, the complex structure of coal is reduced to a collection of matrix blocks of simple geometries (e.g. slides, matches, parallelepiped, cubes or spheres) separated by fracture voids. The size and shape of the blocks depend on the fracture density and the number of fractures sets [27, 28]. Figure 7 represents the geometry model with three sets of cleats. Each set of fracture is defined by an aperture $h_i$ and a spacing $w_i$.

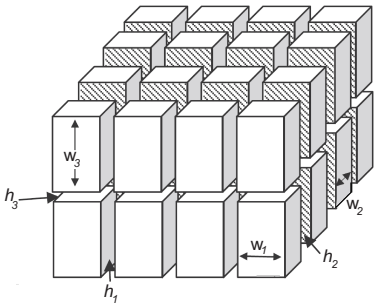


Figure 7: Geometry model with three sets of cleats. *After* [27].

The fractured rock is therefore a dual system. The mechanical behaviour of the fractured rock is analogous to a series of two springs (Figure 8). The spring standing for the fractures is non-linear and initially the softest. When the system is compressed, the soft spring will undergo the first deformations. Then, once fractures are nearly closed, the stiffness tends to the one of the matrix.

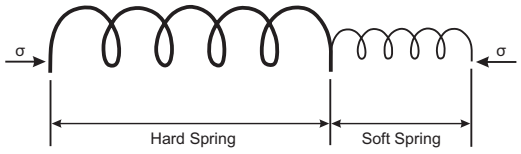


Figure 8: Analogy with two springs in series. *After* [29].

### 3.1. Matrix

The coal matrix is considered isotropic. Therefore, only two elastic parameters are required to define the elastic constitutive tensor. The Young's modulus of the matrix is denoted by $E_m$ and the Poisson's ratio by $\nu_m$. Some authors [30] mentioned orthotropy after mechanical tests on small coal cubes. This may be caused by the presence of fractures at a lower scale. Indeed, it is assumed that coal orthrotropy is induced by the presence of different sets of fractures and the matrix is therefore considered isotropic.

### 3.2. Fractures

A fracture is a discontinuity described by a shear and a normal stiffness, respectively $K_s$ and $K_n$ [31, 32]. These properties depend on the geometry of the asperities of contact between the two rough walls. Due to the rearrangement of these asperities, the normal stiffness increases with the decrease of the normal fracture aperture. The change of normal stiffness for a given mated fracture is evaluated using the empirical model proposed by Bandis [33]:

$$K_n = \frac{K_n^0}{(1 - \frac{u_n}{u_n^{max}})^2} \tag{14}$$

where $u_n = h_0 - h$ is the normal displacement with $h_0$ and $h$ respectively the initial and the current fracture apertures. $K_n^0$ is the normal stiffness corresponding to a zero displacement. The maximal displacement $u_n^{max}$ is a given ratio of the initial aperture. From Equation 14, the stiffness is increasing rapidly when the normal displacement tends to the maximal displacement allowed.

### 3.3. Equivalent continuum

Globally, combining some isotropic matrix blocks with three orthogonal sets of fractures, the material behaviour is orthotropic. In this case, there are 9 independent elastic parameters: $E_1$, $E_2$, $E_3$, $\nu_{12}$, $\nu_{13}$, $\nu_{23}$, $G_{12}$, $G_{13}$ and $G_{23}$ [34, 35]. The compliance tensor is then given in the axes of orthotropy by:

$$D_{ijkl} = \begin{bmatrix} \frac{1}{E_1} & -\frac{\nu_{21}}{E_2} & -\frac{\nu_{31}}{E_3} & 0 & 0 & 0 \\ -\frac{\nu_{12}}{E_1} & \frac{1}{E_2} & -\frac{\nu_{32}}{E_3} & 0 & 0 & 0 \\ -\frac{\nu_{13}}{E_1} & -\frac{\nu_{23}}{E_2} & \frac{1}{E_3} & 0 & 0 & 0 \\ 0 & 0 & 0 & \frac{1}{2G_{12}} & 0 & 0 \\ 0 & 0 & 0 & 0 & \frac{1}{2G_{13}} & 0 \\ 0 & 0 & 0 & 0 & 0 & \frac{1}{2G_{23}} \end{bmatrix} \tag{15}$$

Due to the symmetry of the tensor, the following equality must be satisfied:

$$\frac{\nu_{ij}}{E_i} = \frac{\nu_{ji}}{E_j} \tag{16}$$

Orthotropic coordinate axes may not correspond to the global coordinate axes. In this case, because the constitutive law is formulated in the orthotropic axes, a change of coordinate reference system has to be computed using a rotation matrix $R_{ij}$ which depends on three angles (e.g. Euler's angles) corresponding to rotations relative to the three global axes. To obtain the elastic strain tensor rate in the orthotropic axes ($^\diamond$) from the one expressed in the global axes, the change of reference system is then defined as

$$^\diamond\dot{\varepsilon}_{ij} = R_{ik} R_{jl} \dot{\varepsilon}_{kl} \tag{17}$$

Once the stress state is calculated in the orthotropic axes, it is reformulated in the global axes by reversing the rotation:

$$\tilde{\sigma}_{kl} = R_{ki} R_{lj} {}^\diamond\tilde{\sigma}_{ij} \tag{18}$$

Elastic parameters mentioned in Equation 15 are determined based on the concept of equivalent continuum medium [36]. By analogy with two springs in series, the Young's modulus of the fractured rock in the direction $i$ is calculated as follows[1] [37]:

$$\frac{1}{E_i} = \frac{1}{E_m} + \frac{1}{(K_n)_i \cdot w_i} \tag{19}$$

where $i$ may be any of the three directions of the fractures sets.

The equivalent Poisson's ratios are obtained by:

$$\nu_{ij} = \frac{E_i}{E_m} \cdot \nu_m \tag{20}$$

Finally, the equivalent shear modulus in the plane defined by the directions $i$ and $j$ is estimated by[1]:

$$\frac{1}{G_{ij}} = \frac{1}{G_m} + \frac{1}{(K_s)_i \cdot w_i} + \frac{1}{(K_s)_j \cdot w_j} \tag{21}$$

In fact, as these elastic parameters depend on the non-constant normal stiffness of the fractures and/or the widths of the matrix blocks, the elastic law is non-linear. Figure 9 compares the numerical results of a triaxial test performed on homogeneous and fractured rocks. The homogeneous rock is modelled with constant elastic moduli corresponding to the matrix blocks of the fractured rock. The deviatoric stress evolution with the strain is obviously linear. For the fractured rock, modelled by the equivalent continuum, the initial stiffness is initially lower because of the fractures. Then, while the fractures are closing, the stiffness of the rock tends to the one of the intact rock. The deviatoric stress evolutions are then parallel.

The change of cleat aperture $h$ in the direction $i$ due to the change of normal stress in this direction ($\tilde{\sigma}_{ii}$) is the normal displacement estimated with[1]

$$\dot{h}_i = \frac{\tilde{\sigma}_{ii}}{(K_n)_i} \tag{22}$$

where stresses are positive in traction. Without considering the possibility of dilatance, the shear displacement does not modify

[1] Einstein summation notation is not used in this equation, *i.e* repeated indices do not have to be summed.

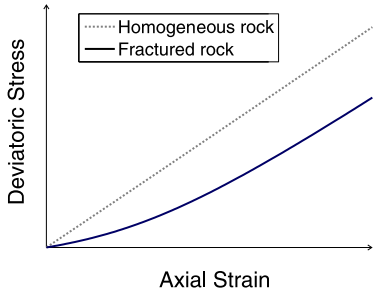


Figure 9: Comparison between homogeneous and equivalent continua.

the cleat aperture. The total change of cleat aperture is then simply given by Equation 22. The total change of the width of one unit including one matrix block and one cleat is the sum of the cleat aperture and the block width changes[1]:

$$\dot{w}_i + \dot{h}_i = (w_i + h_i) \cdot \dot{\varepsilon}_{ii} \tag{23}$$

Therefore, the change of the matrix width appearing in Equations 19 and 21 is given by[1]:

$$\dot{w}_i = (w_i + h_i) \cdot \dot{\varepsilon}_{ii} - \dot{h}_i \tag{24}$$

## 4. Hydraulic model

Usually, coal deposits are aquifers and the methane is maintained adsorbed within the coal matrix by the hydrostatic pressure. The CBM production consists therefore to generate a pressure drop by dewatering the cleats network [38]. Then, gas molecules diffuse in the matrix to reach the cleats which are preferential pathways [39].

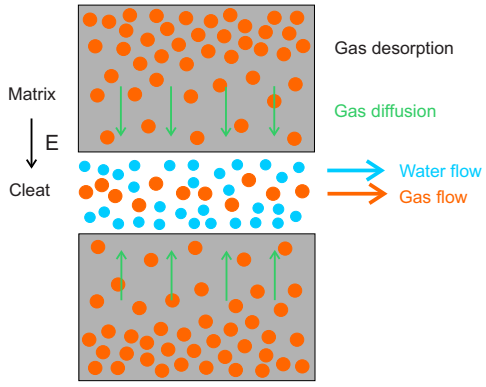


Figure 10: Conceptual hydraulic model.

This section presents a hydraulic model for the modeling of CBM production. The mass balance equations written above involve different variables which are linked to the main variables of the problem through some constitutive and equilibrium equations. Similarly to the mechanical problem, the macroscopic hydraulic model is enriched from the microscale. In this purpose, a dual-porosity approach is adopted, requiring a mass transfer between the matrix and the cleats as presented in the gas mass balance Equations 11 and 12.

### 4.1. Constitutive equations

Different variables such as densities, degrees of saturation or fluid flows appear in the balance equations presented above. All these variables depend on the main variables of the problem, the water pressure and the gas pressure.

#### 4.1.1. Liquid density variation

If the compressibility of the liquid phase is not neglected, its density $\rho_w$ varies with pressure $p_w$. The liquid water bulk density evolves according to:

$$\rho_w = \rho_{w_0} \left(1 + \frac{p_w - p_{w_0}}{\chi_w}\right) \tag{25}$$

where $\rho_{w_0}$ is the liquid density at the pressure $p_{w_0}$ and $1/\chi_w$ is the liquid compressibility. At $20°C$, $1/\chi_w = 5 \cdot 10^{-10} Pa^{-1}$.

#### 4.1.2. Gas density variation

The classical ideal gas equation of state is used to write the gas densities as

$$\rho_g = \frac{M_g}{RT} p_g \tag{26}$$

where $R$ is the universal gas constant ($8.3143\ J/mol \cdot K$), $T$ is the absolute temperature, $M_g$ is the molecular mass of the gas ($0.016\ kg/mol$ for methane) and $p_g$ is the gas pressure either in the fractures ($p_{g,f}$) or in the matrix ($p_{g,m}$)

#### 4.1.3. Multiphase flow model

In porous media, flow occurs in the pore spaces between the solid skeleton. However, the pore-scale representation is not suitable to simulate flow over large domains. Modeling the hydraulic behaviour of coal, it is assumed advective flows take place inside a representative regular macroporosity, the fractures network. Darcy's equation is therefore employed using a permeabilty coefficient which is function of the apertures of the fractures and the widths of the blocks. Inside the microporosity of the matrix blocks, diffusive flows are computed with a Fick's law using a diffusive coefficient.

*Advective flows in the cleats.*

From the experiments performed by Darcy on a column of sand [40], it follows that the flow $q[m/s]$ through a porous medium is proportional to the total pressure drop. This law is valid only for a slow and viscous flow, *i.e.* at small Reynolds numbers (Stokes' flow). In one dimension ($s$ is the distance in the one-dimension system), it writes:

$$q = -\frac{k}{\mu} \frac{\mathrm{d}p}{\mathrm{d}s} \tag{27}$$

where the linear coefficient $k[m^2]$ is called the *intrinsic* or *absolute permeability* of the porous medium. The complex geometry of the porous medium can be therefore replaced by a permeability parameter, what makes Darcy's law very suitable for a continuum macroscopic modeling. In the case of fractured rocks, the permeability may be determined theoretically as a function of the fracture aperture. The permeability through

a set of parallel fractures of equal aperture, oriented parallel to flow direction, is given by [28, 41]:

$$k = \frac{h_b^3}{12w} \tag{28}$$

where $h_b$ is the hydraulic aperture and $w$ is the fracture spacing (Figure 11). In fact, this results can be obtained from the Navier-Stokes Equations [42]. Indeed, the flow through a single fracture represented by two plates is:

$$q_f = -\frac{h_b^2}{12} \cdot \frac{1}{\mu} \frac{\mathrm{d}p}{\mathrm{d}s} \tag{29}$$

Thus, the total flow $Q[m^3/s]$ between the two plates is:

$$Q = q_f \cdot h_b \cdot w = -\frac{h_b^3 w}{12} \frac{1}{\mu} \frac{\mathrm{d}p}{\mathrm{d}s} \tag{30}$$

Considering a section $A$ with $n$ fractures, the permeability through the section is:

$$k = \frac{n}{A} \cdot \frac{h_b^3 w}{12} \tag{31}$$

where $A = n \cdot (w + h_b)^2 \simeq nw^2$ as $w \gg h_b$. Substituting this value in Equation 31, the permeability through the fractured medium is, as announced, given by Equation 28.

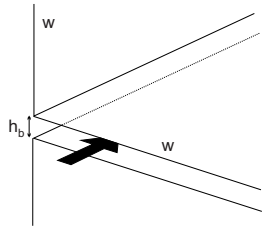


Figure 11: Fluid flow through a cleat. *Modified from* [27].

Superposing three orthogonal sets of cleats, the anisotropic permeability tensor in the axes of these three sets is:

$$k_{ij} = \begin{bmatrix} \frac{1}{12}\left(\frac{h_{b_2}^3}{w_2} + \frac{h_{b_3}^3}{w_3}\right) & 0 & 0 \\ 0 & \frac{1}{12}\left(\frac{h_{b_1}^3}{w_1} + \frac{h_{b_3}^3}{w_3}\right) & 0 \\ 0 & 0 & \frac{1}{12}\left(\frac{h_{b_1}^3}{w_1} + \frac{h_{b_2}^3}{w_2}\right) \end{bmatrix} \tag{32}$$

Barton presented an empirical relationship between hydraulic apertures $h_b$ and mechanical apertures $h$ [43]:

$$h_{b_i} = \begin{cases} \dfrac{h_i^2}{JRC^{2.5}}, & \text{if } h_i \geqslant h_{b_i} \text{ and } JRC > 0. \\ h_i, & \text{otherwise.} \end{cases} \tag{33}$$

where the unit of apertures is micron and JRC is the Joint Roughness Coefficient [44]. A zero JRC represents smooth plane surfaces, in this case the hydraulic aperture is the mechanical one.

Furthermore, the porosity from fractures can be written as [45]:

$$\phi_f = \frac{h_1}{w_1} + \frac{h_2}{w_2} + \frac{h_3}{w_3} \tag{34}$$

Under isotropic conditions, the porosity is therefore $\phi_f = \frac{3h}{w}$. Assuming smooth fractures, this porosity is substituted in Equation 28 to give:

$$k = \frac{1}{96} w^2 \phi_f^3 \tag{35}$$

Thence, the permeability change with respect to a reference state (subscript 0) writes:

$$\left(\frac{k}{k_0}\right) = \left(\frac{w}{w_0}\right)^2 \left(\frac{\phi_f}{\phi_{f_0}}\right)^3 \tag{36}$$

Considering the matrix size change as negligible compared to porosity change ($w \approx w_0$), then Equation 36 can be simplified as:

$$\left(\frac{k}{k_0}\right) = \left(\frac{\phi_f}{\phi_{f_0}}\right)^3 \tag{37}$$

This relationship is commonly used and widely accepted in petroleum industry to describe the permeability change with respect to porosity variation [46, 47]. It is supported by experimental results on fractured rocks [48]. However, since the porosity is a scalar variable, the anisotropy vanishes in the absolute permeability evolution. Moreover, some experimental results have shown Equation 37 may not be applicable for most coalbeds [49]. For this reason, it is preferable to keep a direct relation between the permeability and the cleats apertures. Therefore, contrary to many permeability models described in the literature, Equation 37 is not used in this paper to model coalbed methane flows.

Generally, gas and water flows are simultaneously encountered in the cleats and it is therefore necessary to extend the model to unsaturated conditions. To this purpose, the widely-used concept of relative permeability $k_r$ is introduced to account for the reduction in permeability between partially and fully saturated conditions. Then, advective flows of the liquid and gas phases are respectively:

$$q_{l_i} = -\frac{k_{rw} \cdot k_{ij}}{\mu} \frac{\partial p_w}{\partial x_j} \tag{38}$$

and

$$q_{g_i} = -\frac{k_{rg} \cdot k_{ij}}{\mu} \frac{\partial p_g}{\partial x_j} \tag{39}$$

The relative permeability curves $k_{rw}$ and $k_{rg}$ in porous media are often expressed with Corey functions [50]. It was demonstrated the same mathematical expressions are suitable for gas and water flowing in the cleat system [51]. These expressions are:

$$k_{rw} = (S_r^*)^{\eta+1+\frac{2}{\lambda}} \tag{40}$$

$$k_{rg} = (1 - S_r^*)^{\eta} \cdot \left[1 - (S_r^*)^{1+\frac{2}{\lambda}}\right] \tag{41}$$

where $S_r^*$ is the normalized wetting phase saturation defined below, $\lambda$ is a cleat size distribution index controlling the difference in the cleat size and $\eta$ is a parameter taking into account the effect of the tortuosity on the flow path (Figure 12).

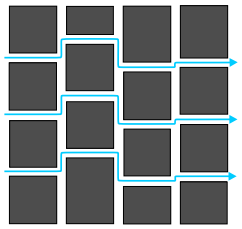

Figure 12: Effect of the tortuosity on the flow path. *Modified from* [51].

Relative permeabilities are represented in Figure 13 for different values of $\eta$ and $\lambda$. For instance, coal cleats become more tortuous with the increase of $\eta$ and the relative permeabilities for both water and gas phases decrease.

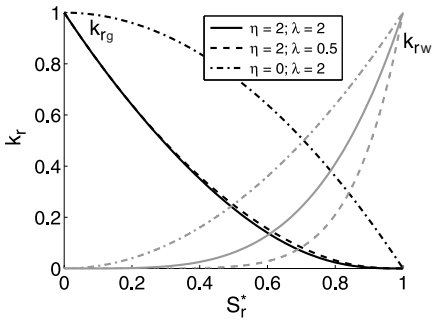


Figure 13: Effect of tortuosity and cleat size distribution index on relative permeability curves.

These relative permeability Equations 40 and 41 require to define a retention curve to link the degree of saturation and the capillary pressure $p_c$. In 1964, the Brooks and Corey empirically proposed a capillary pressure model [52] which has now a solid theoretical base [53] since the development of the fractal geometry [54]. Brooks and Corey proposed the following function:

$$p_c(S_r) = p_e \cdot (S_r^*)^{\frac{-1}{\lambda}} \tag{42}$$

where $p_e$ is the entry capillary pressure and $S_r^*$ is the normalized wetting phase saturation defined by:

$$S_r^* = \frac{S_r - S_{r,res}}{1 - S_{r,res} - S_{r_g,res}} \tag{43}$$

with $S_{r,res}$ and $S_{r_g,res}$ the residual water and gas saturations. If the residual water and gas contents are considered constant while the porosity evolves, the mass conservation of these residual fluids implies

$$S_r^* = \frac{S_r - S_{r,res_0}\left(\frac{\phi}{\phi_0}\right)^{-1}\left(\frac{\rho_w}{\rho_{w_0}}\right)^{-1}}{1 - S_{r,res_0}\left(\frac{\phi}{\phi_0}\right)^{-1}\left(\frac{\rho_w}{\rho_{w_0}}\right)^{-1} - S_{r_g,res_0}\left(\frac{\phi}{\phi_0}\right)^{-1}\left(\frac{\rho_g}{\rho_{g_0}}\right)^{-1}} \tag{44}$$

In fact, the total amount of residual contents may change with the porosity as a result of pore size variation. To represent experimental data, the residual saturations expressions are improved by introducing some exponents $n_{rw}$ and $n_{rg}$ [51]:

$$S_{r,res} = S_{r,res_0}\left(\frac{\phi}{\phi_0}\right)^{-n_{wr}}\left(\frac{\rho_w}{\rho_{w_0}}\right)^{-1} \tag{45}$$

$$S_{r_g,res} = S_{r_g,res_0}\left(\frac{\phi}{\phi_0}\right)^{-n_{gr}}\left(\frac{\rho_g}{\rho_{g_0}}\right)^{-1} \tag{46}$$

*Diffusive flows.*

Fick's law [55] is the most popular approach to evaluate diffusive flow. It states the flow is directly proportional to the concentration gradient. The flow in the direction $i$ for the species $\alpha$ is given by:

$$J_{\alpha i} = -D_\alpha \frac{\partial C_\alpha}{\partial x_i} \tag{47}$$

Equation 47 is known as the Fick's first law. In this equation, the determination of the phenomenological coefficient $D_\alpha$ $[m^2/s]$ is naturally the most critical part of the equation. Fick's second law can be derived from Fick's first law and mass conservation, this law is written as follows:

$$\frac{\partial C_\alpha}{\partial t} = D_\alpha \frac{\partial^2 C_\alpha}{\partial x_i^2} \tag{48}$$

In porous media, as real pores are generally of various diameters and twisted, the path for diffusion of the molecules within the pores is tortuous. A reasonable approximation for the effective diffusion coefficient of the species $\alpha$ through $\beta$, is given by [56]:

$$D_\beta^{\alpha\,\divideontimes} = \phi\, \Lambda\, D_\beta^\alpha \tag{49}$$

in which $\Lambda$ is the tortuosity defined as the square of the ratio between the straight line distance and the effective length covered by the molecule. It is therefore an obstruction factor lower or equal to one which attempts to account for the longer distance traversed in the pores.

Fick's law will be used in the dual-porosity approach (section 4.3) to account in the gas transfer between matrix and cleats that desorption is not instantaneous. Fick's law is also used to express the diffusive flow of dissolved gas in water in the cleats:

$$J_{l\,i}^g = -D_l^{g\,\divideontimes} \frac{\partial}{\partial x_i}\left(\frac{\rho_g^d}{\rho_w}\right) \tag{50}$$

For methane dissolved in water, the diffusion coefficient is 1.84E-9 $m^2/s$. By not considering water vapour, all flows appearing in the mass balance Equations 10 to 11 are therefore defined.

### 4.2. Equilibrium equations

For closure of the mass balance equations, some restrictions are also required to link the different phases of each species (Figure 14).

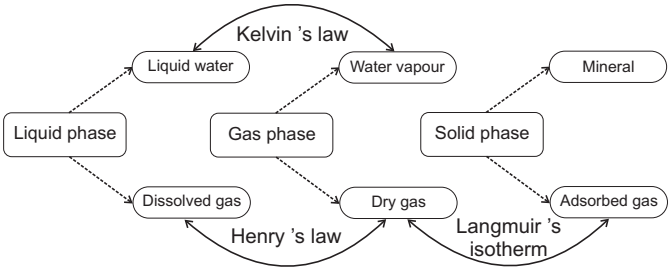


Figure 14: Phases, species and equilibrium restrictions.

#### 4.2.1. Henry's law

Assuming a thermodynamic equilibrium between the dissolved gas and the dry gas, the density of the dissolved gas may be obtained with the Henry's law [57]:

$$\rho^{d}_{g,f} = H_g \rho_{g,f} \tag{51}$$

Hence, Henry's coefficient $H_g$ allows determining the dissolved gas volume in the water. Its value depends on gas type and temperature. For methane dissolved in water at standard conditions, $H_g = 0.0347$ [58].

#### 4.2.2. Langmuir's isotherm

Adsorption isotherm is the most widely used technique to describe gas adsorption, it is a relation giving the maximal quantity of adsorbed gas as a function of gas pressure at a given temperature. The Langmuir model [59] is extensively used for describing methane adsorption/desorption on coal because of its ability to close fit experimental data. The Langmuir model is a special form of the multilayer Brunnauer-Emmet-Teller (BET) model for which each adsorbate molecule in the first layer serves as an adsorption site for an adsorbate molecule into the second layer, the second layer for the third layer, and so on (Figure 15) [60].

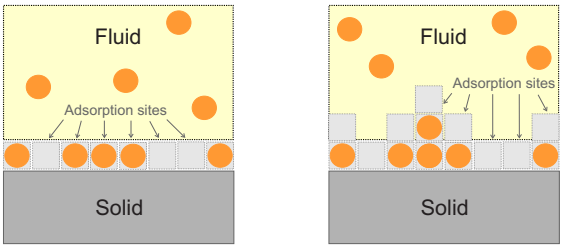


(a) Langmuir (b) BET

Figure 15: Sketches of the Langmuir and BET models.

The Langmuir's isotherm may be derived considering the following equilibrium equation:

$$M_g + O- \rightleftharpoons O - M_g \tag{52}$$

where $M_g$ represents the gas phase molecules, $O-$ the vacant surface sites and $O - M_g$ the species adsorbed on the surface. At equilibrium, the rate of forward reaction is equal to rate of backward reaction and the corresponding equilibrium constant $K$ is given by:

$$K = \frac{[O - M_g]}{[M_g] \cdot [O-]} \tag{53}$$

$[O - M_g]$ and $[O-]$ are respectively proportional to the surface coverage of adsorbed molecules $\theta$ and the vacant surface $1 - \theta$. As $[M_g]$ is proportional to the pressure of gas $p$, then a new equilibrium constant writes

$$K' = \frac{\theta}{(1-\theta) \cdot p} \tag{54}$$

Hence, the surface coverage is:

$$\theta = \frac{K' \cdot p}{1 + K' \cdot p} \tag{55}$$

in which $K'$ depends on temperature and enthalpy change for the process. The total adsorbed volume $V_{g,Ad}$ equals $\theta \cdot V_L$, where $V_L$ is the monolayer adsorption capacity, it represents the volume adsorbed for an infinite pressure. The total adsorbed volume is finally written as follows:

$$V_{g,Ad} = \frac{V_L \cdot p}{P_L + p} \tag{56}$$

where $P_L$ is the Langmuir pressure corresponding to $\frac{1}{2}V_L$. These two parameters, $P_L$ and $V_L$, are used to control the shape of the curve to best fit some experimental data. Figure 16 shows how well the Langmuir's model can fit some experimental results obtained for different coal basins from Belgium [61]. Langmuir's parameters of these curves are given below.

| Basin | $V_L\ [m^3/t]$ | $P_L\ [MPa]$ |
|---|---|---|
| Campine | 22.75 | 0.95 |
| Borinage | 26 | 1.2 |
| Borinage bis | 28 | 0.8 |
| Liège | 32 | 0.9 |

Table 1: Langmuir's parameters fitting adsorption data published by [61].

$V_{g,Ad}$ and $V_L$ are not strictly volumes but volumes of stored gas at standard conditions per unit of mass of coal. The density of the gas adsorbed on the coal matrix is therefore evaluated as

$$\rho_{g,Ad} = \rho_{g,std} \cdot \rho_c \cdot V_{g,Ad} \tag{57}$$

where $\rho_{g,std}$ is the gas density at standard conditions and $\rho_c$ is the coal density. To write the gas density in the matrix, Equation 56 is introduced in Equation 57 and rearranged with the gas equation of state (Equation 26). Given a reservoir pressure $p_{res}$, the gas density in the matrix must tend to:

$$\rho^{lim}_{g,m} = \frac{RT}{M_g} \cdot \rho_{g,std} \cdot \rho_c \frac{V_L \cdot p_{res}}{P_L + p_{res}} \tag{58}$$

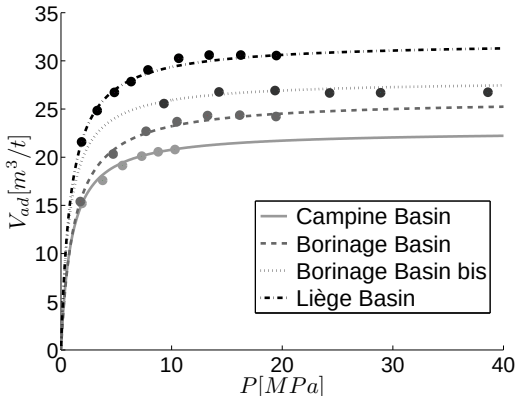


Figure 16: Langmuir's isotherm fitting with data published by [61].

where the reservoir pressure is evaluated with the following equivalent pressure:

$$p_{res} = S_r p_w + (1 - S_r) p_{g,f} \tag{59}$$

In fact, if the maximal amount of gas is not stored at the beginning of the production, *i.e.* the initial gas content is under the isotherm (Figure 4), then the first drop of the reservoir pressure does not lead to desorption and the gas pressure in the matrix remains constant. Desorption starts once the Langmuir's isotherm is reached, *i.e.* at the critical reservoir pressure $p_{res}^{crit}$:

$$p_{res}^{crit} = \frac{p_{g,m}^0 \cdot P_L}{\left(\frac{RT}{M_g} \cdot \rho_{g,std} \cdot \rho_c \cdot V_L - p_{g,m}^0\right)} \tag{60}$$

From this pressure, it is the role of the shape factor presented in the following section to evaluate the transfer from the matrix to the fractures.

### *4.3. Dual-porosity approach*

Naturally-fractured reservoirs may be treated as dual-porosity media. The drainage rate per unit bulk volume from matrix to fractures was idealized by Barenblatt and later by Warren and Root as [23, 62]:

$$E = \Psi \frac{\rho k}{\mu} (p_m - p_f) \tag{61}$$

where the parameter $\Psi$ is a shape factor with the dimension of reciprocal area, $\mu$ is the dynamic viscosity and $p_m$ and $p_f$ are respectively the matrix and fracture pressures. In the case of coal, adsorption isotherm has to be considered in the equation. Indeed, the motor of the transfer is the difference between the matrix pressure and the limit matrix pressure (Figure 17). This limit matrix pressure is the pressure towards which the pressure tends given the pressure in the fractures, it is determined *via* Equation 58.

As the drainage rate results from a diffusion process, a Fickian form is employed to give

$$E = \Psi D_m^g M_g (C_{g,m} - C_{g,m}^{lim}) \tag{62}$$

$$= \Psi D_m^g \frac{M_g}{RT} (p_{g,m} - p_{g,m}^{lim}) \tag{63}$$

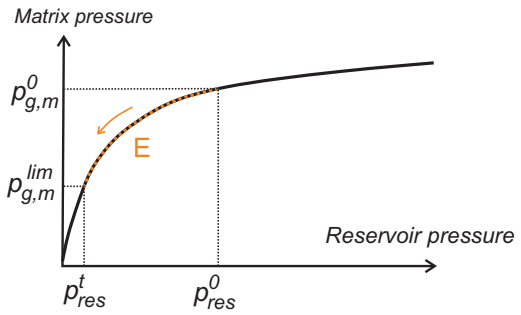


Figure 17: Mass exchange process between cleats and matrix.

The shape factor $\Psi$ aims to take into account the geometry of the matrix block in the release of gas (Figure 18).

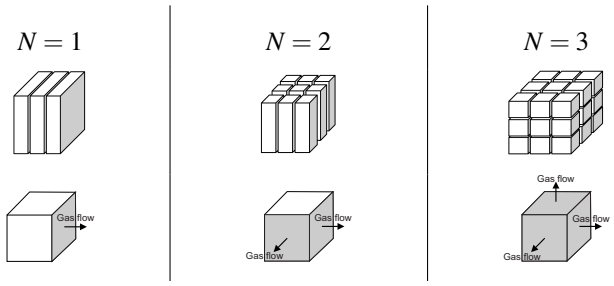


Figure 18: Influence of the geometry on the release process.

Warren and Root obtained the following expression of the shape factor:

$$\Psi = \frac{4N(N+2)}{w^2} \tag{64}$$

where $N$ is the number of sets of fractures (1, 2 or 3) and $w$ is the fracture spacing. According to Kazemi, the shape factor should be evaluated as [63]:

$$\Psi = 4 \left( \frac{1}{w_1^2} + \frac{1}{w_2^2} + \frac{1}{w_3^2} \right) \tag{65}$$

Kazemi's formula is perhaps the most used in commercial reservoir simulators such as Eclipse [64]. However, this shape factor probably does not represent the most realistic pressure distribution in the matrix. Observations were made in the literature on the need to multiply the Kazemi's shape factor by a factor 2 or 3 to correspond to experimental results [65]. Actually, Warren and Root's model and Kazemi's one are two extreme bounds, others authors derived intermediate rates of change flow [66, 67, 68, 69, 70]. For example, based on a Fourier finite sine transform and integration, Coats derived a shape factor doubled compared to Kazemi [66]. Based on the same method, Lim and Aziz developed a shape factor formula assuming the flow obeys Darcy's law in the matrix with constant fracture pressure [70].

In order to understand the assumptions under the use of a shape factor, the procedure is shortly developed assuming the flow obeys Fick's first law (Equation 47) in the matrix. From Fick's second law (Equation 48), the concentration distribution

satisfies in one dimension:

$$\frac{\partial C}{\partial t} = D_m^g \frac{\partial^2 C}{\partial x^2} \tag{66}$$

The following boundary conditions ($N = 1$) are considered:

- At $t = 0$, we have $C = C^0$ for $-\frac{w}{2} \leqslant x \leqslant \frac{w}{2}$
- For $t > 0$, we have $C = C^{lim}$ for $x = -\frac{w}{2}$ and $x = \frac{w}{2}$

If the matrix is initially at a uniform concentration $C^0$ and the concentration at the boundary is maintained constant at $C^{lim}$, solution of Equation 66 is expressed by the Crank analytical solution [71]:

$$\frac{\bar{C}_m - C^0}{C^{lim} - C^0} = 1 - \sum_{n=0}^{\infty} \frac{8}{(2n+1)^2\pi^2} \exp\left(\frac{-(2n+1)^2\pi^2 D_m^g\, t}{w^2}\right) \tag{67}$$

where $\bar{C}_m$ is the average concentration in the matrix at time $t$. Taking the first term in the infinite summation series, Equation 67 is approximated by:

$$\frac{\bar{C}_m - C^0}{C^{lim} - C^0} = 1 - 0.81 \exp\left(\frac{-\pi^2 D_m^g\, t}{w^2}\right) \tag{68}$$

Differentiating this equation with respect to time yields to

$$\frac{1}{C^{lim} - C^0}\frac{\partial \bar{C}_m}{\partial t} = \frac{\pi^2 D_m^g}{w^2} 0.81 \exp\left(\frac{-\pi^2 D_m^g\, t}{w^2}\right) \tag{69}$$

$$= \frac{\pi^2 D_m^g}{w^2}\left[1 - \frac{\bar{C}_m - C^0}{C^{lim} - C^0}\right] \tag{70}$$

where Equation 70 is not time-dependent. The time dependence is eliminated using only the first term of the series. Figure 19 shows the approximate solution is in good agreement with the analytical solution except in the first dimensionless times.

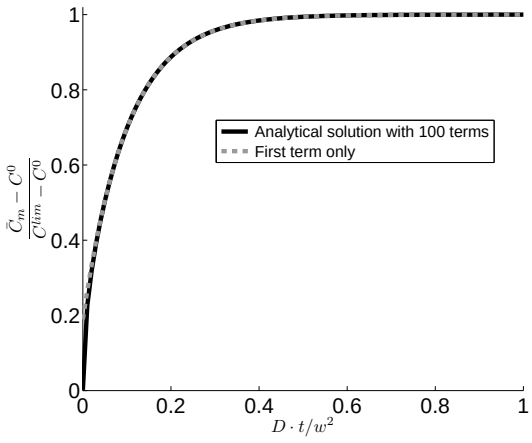


Figure 19: Crank solution for diffusion ($D$ coefficient) in a plane (width $w$) and its approximation.

Thence, we can write:

$$\frac{\partial \bar{C}_m}{\partial t} = \frac{\pi^2 D_m^g}{w^2}(C^{lim} - \bar{C}_m) \tag{71}$$

The rate of the matrix-fracture transfer can be related to the rate of mass accumulation in the matrix as follows:

$$E = -M_g \frac{\partial \bar{C}_m}{\partial t} \tag{72}$$

Substituting Equation 71 in Equation 72 and comparing with Equation 62, we finally find a shape factor of $\frac{\pi^2}{w^2}$ for $N = 1$. For the 3D case, similar developments yields to [70]:

$$\Psi = \pi^2\left(\frac{1}{w_1^2} + \frac{1}{w_2^2} + \frac{1}{w_3^2}\right) \tag{73}$$

| | $N=1$ | $N=2$ | $N=3$ |
|---|---|---|---|
| Warren and Root | 12 | 32 | 60 |
| Kazemi | 4 | 8 | 12 |
| Coats | 8 | 16 | 24 |
| Lim and Aziz | $\pi^2$ | $2\pi^2$ | $3\pi^2$ |

Table 2: Dimensionless shape factor values ($\Psi\, w^2$) from different authors.

Table 2 compares different shape factors from different authors. Values of the shape factors depend on the block geometry which is assumed. A regular microscale configuration has to be considered when evaluating macroscopically the transfer between the two porosity systems. Moreover, Equation 67 suggests differentiation with respect to time will not eliminate the dependence from time in the actual shape factor, as approximated by all the authors referred in Table 2 considering a pseudo-steady state[2]. As a result, the mass transfer between cleat and matrix is approximated for the transient period before the establishment of the pseudo-steady state, as illustrated by the Figure 19.

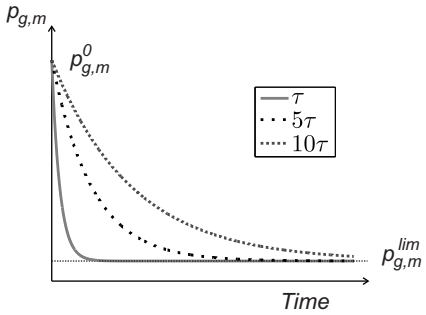


Figure 20: Comparison of the matrix gas pressure evolutions for different τ.

Finally, the differential equation governing the matrix gas pressure evolution is

$$\dot{p}_{g,m}(t) = -\Psi D_g^m \cdot \left(p_{g,m}(t) - p_{g,m}^{lim}(t)\right) \tag{74}$$

[2]Change in the rate of pressure with time is constant at every point.

Given an initial gas matrix pressure $p^0_{g,m}$ and assuming a constant fracture pressure, the mathematical solution of this equation is a decreasing exponential function in the form:

$$p_{g,m}(t) = \left(p^0_{g,m} - p^{lim}_{g,m}\right) \cdot \exp\left(\frac{-t}{\tau}\right) + p^{lim}_{g,m} \tag{75}$$

where $\tau = \dfrac{1}{\Psi D^m_g}$ is the sorption time. It allows to account for the combined impacts of cleat spacing and gas diffusion in coal matrix on gas flow. This sorption time corresponds to the time required to desorb 63.2% of the gas which can be produced following a given pressure drop in the fractures. Indeed, the part of the gas already released at any time $t$ is given by:

$$1 - \exp\left(\frac{-t}{\tau}\right) \tag{76}$$

Thence, replacing $t$ with $\tau$ leads to $1 - \exp(-1) = 63.2\%$.

Figure 20 compares the evolutions of the matrix pressure for different values of the sorption time. The lower is the sorption time and the faster the gas is desorbed.

## 5. Hydro-mechanical model

The mechanical and the hydraulic laws presented above should not be treated separately because of couplings, this is especially true for coalbed methane production. Indeed, the reservoir depletion compacts the rock and decreases the permeability. However, matrix shrinkage following the gas desorption from the coal matrix may increase the cleat aperture and thus the permeability [11].

### 5.1. Hydraulic - mechanical coupling

The influence of the hydraulic problem on the mechanical one is of two kinds. First, the mechanical behaviour of porous media is not entirely controlled by the total stress, it is also influenced by the presence of fluids in the pores. In this purpose, the concept of effective stress [72] is introduced. Secondly, sorption or desorption induces a swelling or a shrinkage of the matrix.

#### 5.1.1. Effective stress approach

Terzaghi was the first to notice the role of the pore fluid pressure in rock and soil deformation [73]. After experiments with sand, clay and concrete, he concluded the change in bulk volume was only influenced by the difference between the confining pressure and the pore water pressure, *i.e. effective stress*. It is the stress acting effectively between the solid grains. In order to introduce the material compressibility in the effective stress definition, Biot proposed to scale down the effect of the water pressure with the so-called Biot's coefficient [74]. For partially saturated conditions, Bishop extended Terzaghi's definition of the effective stress by combining both liquid and gas pressures [75]. The principle of effective stress has also been investigated for fractured media [76].

It is presumed that partial saturation and compressibility effects can be considered together. Moreover, an average fluid pressure composed of the pressure of each fluid weighted by their degree of saturation is used in the same way the reservoir pressure is defined in Equation 59 [77]. Thence, the effective stress $\sigma'_{ij}$ is formulated as follows[3]:

$$\sigma'_{ij} = \sigma_{ij} - b_{ij}\left[S_r\, p_w + (1 - S_r)\, p_g\right] \delta_{ij} \tag{77}$$

where $\delta_{ij}$ is the Kronecker symbol[4] and $b_{ij}$ is the Biot's coefficients tensor. Equation 77 is used as the effective stress definition for the double porosity model with the water and gas pressures in the fractures. Biot's coefficients depend on the elastic moduli of the fractured medium and the non-fractured blocks, their expressions are:

$$b_{ij} = \delta_{ij} - \frac{C_{ijkk}}{3K_m} \tag{78}$$

where $K_m$ is the bulk modulus of the matrix blocks.

#### 5.1.2. Swelling/shrinkage

Sorption or desorption induces structural rearrangements within the structure of the coal matrix [78]. As a consequence, a volumetric strain is induced. Figure 21 presents data from different $CO_2$ injection experiments. It appears these data could be modelled fairly accurately using the same mathematical form as the Langmuir's Equation [25]. Moreover, the volumetric sorption-induced strain $\varepsilon_{vs}$ is approximately proportional to the volume of adsorbed gas [47][5]:

$$\varepsilon_{vs} = \beta_\varepsilon \cdot V_{g,Ad} \tag{79}$$

where $\beta_\varepsilon$ is the volumetric strain coefficient. Assuming an isotropic swelling/shrinkage of the matrix, the linear strain in the direction $i$ due to gas adsorption/desorption can be estimated from[1]:

$$\varepsilon_{iis} = \alpha_\varepsilon \cdot V_{g,Ad} \cong \frac{1}{3}\beta_\varepsilon \cdot V_{g,Ad} = \frac{1}{3} \cdot \varepsilon_{vs} \tag{80}$$

where $\alpha_\varepsilon$ is the linear strain coefficient. Indeed[1], $\varepsilon_v = (1 + \varepsilon_{ii})^3 - 1 \cong 3\varepsilon_{ii}$ for small strains. Actually, the linear strain coefficient could be different in every direction. A larger expansion may occur in the direction perpendicular to the bedding plane [79]. However, isotropic conditions have to be assumed in the absence of more information.

### 5.2. Mechanical - hydraulic coupling

The constitutive mechanical model relates effective stress and strain according to

$$\tilde{\sigma}'_{ij} = C_{ijkl}\, \dot{\varepsilon}_{kl} \quad \Leftrightarrow \quad \dot{\varepsilon}_{ij} = D_{ijkl}\, \tilde{\sigma}'_{kl} \tag{81}$$

[3] Definition with soil mechanics convention in which compressive stress is positive.

[4] $\delta_{ij} = 0$ if $i \neq j$ and $\delta_{ij} = 1$ if $i = j$.

[5] In the following, material mechanical convention with positive tensile stress and strain is adopted to be in accordance with the convention of the finite element code.

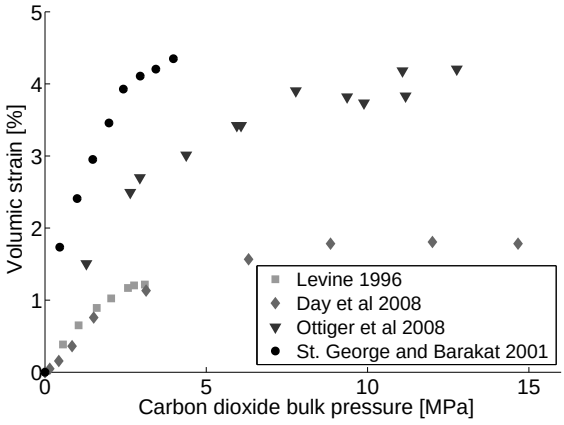


Figure 21: Swelling process during $CO_2$ injection in different coals. *Experimental data from* [25], [80], [81] and [82].

where $\tilde{\sigma}'_{ij}$ is the Jaumann objective effective stress rate and $\dot{\varepsilon}_{ij}$ takes into account sorption-induced strain analogously to thermal expansion of rocks [46]. In practice, based on the principle of superposition, the total linear strain is due to the changes in effective stress and adsorbed gas swelling. In the axes of orthotropy, it writes:

$$\dot{\varepsilon}_{ij_{tot}} = \dot{\varepsilon}_{ij} + \dot{\varepsilon}_{ij_s}\delta_{ij} \tag{82}$$

Thence, the strain rate used in Equation 81 must be

$$\dot{\varepsilon}_{ij} = \dot{\varepsilon}_{ij_{tot}} - \dot{\varepsilon}_{ij_s}\delta_{ij} \tag{83}$$

Thereby, if the displacement imposed by the boundary conditions is null, the swelling strain is totally converted into internal stresses, which are partly traduced in fracture aperture change according to the following equation written for the direction $i$[1]:

$$\dot{h}_i = \frac{\tilde{\sigma}'_{ii}}{(K_n)_i} \tag{84}$$

As permeability evolves with the cleat aperture (Equation 32), the influence of the mechanical aspects on the hydraulic problem is a critical issue. A review of the analytical models used in the literature for the coal permeability evolution with the stress state may be found in [45], where around twenty others models are presented. In fact, many of them are based on the relationship between permeability and porosity presented above (Equation 37). Reservations were expressed when linking the evolution of the permeability tensor to a scalar variable. In our model, by introducing Equation 84 in Equation 32, it is not the case.

## 6. Finite element formulation

The hydro-mechanical model presented is formulated as a series of balance equations which are local equilibria expressed in a differential form. In addition to the balance equations, initial and boundary conditions are necessary to obtain a well-posed problem. To address problems over large domains with a finite element analysis, balance equations must be written in a weak form. Then, the numerical formulation requires to convert continuous time and space into finite time steps and finite elements. Finally, the system of linear equations is solved to give the global solution of the problem. Since the method is extensively developed in many books (see for instance [83]), it is not completely detailed here.

### 6.1. Initial and boundary conditions

While the balance equations represent the equilibrium of the material elementary volume $\Omega$, the boundary conditions are the equilibrium at the external surface of the domain $\Gamma$. Initial conditions are also necessary for model closure, it describes the entire fields of displacements, water pressures and gas pressures to start from. The external traction force per unit area acting on a part of the external surface reads

$$\bar{t}_i = \sigma_{ij} \cdot n_j \tag{85}$$

where $n_i$ is the unit vector normal to the boundary. Similarly, the conditions for prescribed water and gas fluxes are

$$q_w + f_{w_i} \cdot n_i = 0, \text{ and } q_g + f_{g_i} \cdot n_i = 0 \tag{86}$$

where $q_w$ and $q_g$ are the input water and gas masses (positive for inflow) and $f_{w_i}$ and $f_{g_i}$ are internal total fluxes of water and gas species in both liquid and gas phases:

$$f_{w_i} = \rho_w \, q_{l_i} \tag{87}$$

$$f_{g_i} = \rho_{g,f} \, q_{g_i} + \rho^d_{g,f} \, q_{l_i} + S_r \, J^g_{l_i} \tag{88}$$

with the flows $q_{l_i}$, $q_{g_i}$ and $J^g_{l_i}$ defined by Equations 38, 39 and 50.

### 6.2. Weak form of the balance equations

A weak form of the local momentum balance Equation 7 can be obtained considering an admissible virtual velocity field $\delta v_i$, *i.e.* which respects the solid continuity and the boundary conditions. The principle of virtual power implies that, for any admissible virtual velocity, the solid is in equilibrium if internal virtual power $\dot{W}_I$ is equal to external one $\dot{W}_E$:

$$\underbrace{\int_\Omega \sigma_{ij} \, \varepsilon_{ij}[\delta v_i] \, d\Omega}_{\delta \dot{W}_I} = \underbrace{\int_\Omega \rho g_i \, \delta v_i \, d\Omega + \int_\Gamma \bar{t}_i \, \delta v_i \, d\Gamma}_{\delta \dot{W}_E} \tag{89}$$

and because it holds for any $\delta v_i$, the momentum balance Equation 7 and the boundary condition 85, are deduced inside the domain $\Omega$ and for any point on the boundary $\Gamma$.

In the same way, the fluids mass balance equations may be written in a weak form considering some kinematically admissible virtual fluid pressure fields. With $\delta p_w$ the virtual water pressure field, the water mass balance equation reads

$$\underbrace{\int_\Omega \left[ \dot{M}_w \delta p_w - f_{w_i} \frac{\partial}{\partial x_i} (\delta p_w) \right] d\Omega}_{\delta \dot{W}_I} = \underbrace{\int_\Omega Q_w \delta p_w \, d\Omega - \int_\Gamma \bar{q}_w \, \delta p_w \, d\Gamma}_{\delta \dot{W}_E} \tag{90}$$

where $Q_w$ is the water source term and $M_w$ is the total mass of water:

$$M_w = \rho_w \, S_r \, \phi_f \tag{91}$$

Similarly with $\delta p_g$ the virtual gas pressure field, the gas mass balance equation is

$$\underbrace{\int_\Omega \left[ \dot{M}_g \delta p_g - f_{g_i} \frac{\partial}{\partial x_i} (\delta p_g) \right] d\Omega}_{\delta \dot{W}_I} = \underbrace{\int_\Omega Q_g \delta p_g \, d\Omega - \int_\Gamma \overline{q}_g \, \delta p_g \, d\Gamma}_{\delta \dot{W}_E} \tag{92}$$

where $Q_g$ is the gas source term and $M_g$ is the total mass of gas:

$$M_g = \rho_{g,f} \, (1 - S_r) \, \phi_f + \rho^d_{g,f} \, S_r \, \phi_f + \rho_{g,Ad} \tag{93}$$

### 6.3. Discretization

#### 6.3.1. Time

All the balance equations should be verified at any time $t$. However, the continuous time has to be descritized into finite time steps $\Delta t$ in order to solve numerically the boundary value problem for any time $t$. Time derivatives are defined using a fully implicit difference scheme.

#### 6.3.2. Space

The continuum medium is also discretized by finite elements. A coupled finite element is used to model solid bodies [21]. It is an isoparametric element with eight nodes and four integration points. Primary unknowns are the nodal coordinates, each node has 5 degrees of freedom: the two spatial coordinates, the water and fracture gas pressures, and temperature[6]. Note the adsorbed gas pressure is not considered as a nodal variable but as a state variable, it is computed from the fracture pressures. Coordinates and displacements are interpolated over the parent element using shape functions.

### 6.4. Global solution and coupling strategy

Equilibrium is reached when energetically equivalent internal nodal forces are equal to external ones. However, due to the evolution of the loading, it is likely these nodal forces are not balanced at the beginning of any time step. Therefore, generalised degrees of freedom must be corrected to verify the equilibrium. To this purpose, the system of non-linear equations 89 to 92 is transformed into an auxiliary linear problem and solved numerically with a Newton-Raphson scheme. A stiffness matrix is determined at each iteration of the numerical procedure, components of this matrix are computed as the variation of the equivalent nodal forces due to a variation of the generalised coordinates. The off-diagonal terms contain the multi-physical coupling terms, a monolithic (fully coupled) procedure is then adopted. The influence of sorption on the mechanical strain is considered separately, the sorption-induced strain is computed at the beginning of each iteration from the adsorbed gas pressure (which is not a primary unknown but derived from the fracture pressures) and is subtracted from the total strain (Equation 83) to employ the constitutive mechanical law.

[6] Actually, this work is restricted to isothermal conditions. The interested reader may found in [21] the energy balance equation required to solve non-isothermal problems.

## 7. Reservoir modeling

First, in order to illustrate the applicability of the model, a production scenario is tested on a hypothetical cylindrical CBM reservoir. This synthetic simulation allows us to choose a simple history of the well pressure drop in order to highlight the physical phenomena. The reference case is presented and then a parametric and couplings analysis is performed to highlight the influence of the hydro-mechanical couplings and some key parameters on the production profiles. Finally, the model is applied to represent production data obtained from a real production well.

### 7.1. Synthetic reference case

The reservoir is horizontal with initial homogeneous properties. The radius of the reservoir is $400m$ while the uniform thickness of the coal seam is $5m$. The reservoir is modelled in 2D axisymmetric conditions with 3000 (10x300) coupled finite elements. Both water and gas pressures are initially set to $2MPa$ in the fracture system, the reservoir is water saturated. In the matrix system, the gas pressure is set on the Langmuir's isotherm. Isothermal conditions are considered. Concerning the boundary conditions, all boundaries are impermeable to gas except at the well where the pressure $P_{well}$ is decreased from 2 to $0.5MPa$ in 10 days. The differences between this pressure and the proximate water and gas pressures in the reservoir are responsible for water and gas production rates.

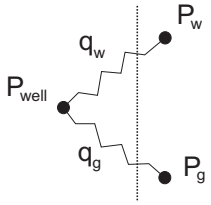


The mass production rates are computed at the boundary as follows [84]:

$$\begin{aligned} q_{w_{well}} &= T \cdot \rho_w \cdot \frac{k_{rw}}{\mu_w} (p_w - P_{well}) \\ q_{g_{well}} &= T \cdot \rho_g \cdot \frac{k_{rg}}{\mu_g} (p_{g,f} - P_{well}) + H_g \cdot \rho_g \frac{f_w}{\rho_w} \end{aligned}$$

where $T[m^3]$ is a transmissibility factor taking into account the characteristics of the well: the borehole radius and the skin factor. Note the dissolved gas is taken into account thanks to the Henry coefficient $H_g$. The outer boundary is not assumed totally impermeable to water, the income water flow is computed according to

$$q_{w_{ob}} = \kappa \cdot (p_{w_0} - p_w) \tag{94}$$

where $\kappa[m^2.s/(kg.Pa)]$ is a penalty coefficient. The value of this coefficient is chosen in order to ensure the water flow at the well is never null, to be closer to real conditions.

Concerning mechanical boundary conditions, lateral displacements on the lateral boundaries are null, vertical displacement on the lower boundary is null and there is an overburden

pressure of $5MPa$ at the top of the coal seam. All others parameters used for the simulation are listed in Table 3. The shape factor is evaluated according to Lim and Aziz's formula (Equation 73). Based on the cleat aperture and the matrix width, the porosity due to fractures is calculated with Equation 34, $\phi_f = 0.3\%$. Then, the initial permeability is calculated with Equation 32, $k = 6.667\text{E-}14\ m^2$. Note the permeability is initially isotropic but evolves anisotropically. The Young's modulus and the Poisson's ratio of the equivalent continuum are, from equations 19 and 20, $E = 1.429GPa$ and $\nu = 0.086$. Finally, the initial Biot's coefficient is equal to 0.86, it is initially isotropic since the stiffness and the aperture of the fractures are equal in the three directions. Then, following Equation 78, it evolves anisotropically.

| Parameters | Values |
|---|---|
| Seam thickness $(m)$ | 5 |
| Reservoir radius $(m)$ | 400 |
| Temperature $(K)$ | 303 |
| Overburden pressure $(Pa)$ | 5E6 |
| Well transmissibility $T$ $(m^3)$ | 1E-12 |
| Penalty coefficient $\kappa$ $(m^2.s/(kg.Pa))$ | 1.5E-19 |
| Coal density $\rho_c$ $(kg/m^3)$ | 1500 |
| Matrix Young's modulus $E_m$ $(Pa)$ | 5E9 |
| Matrix Poisson's ratio $\nu_m$ | 0.3 |
| Matrix width $w$ $(m)$ | 0.02 |
| Cleat aperture $h$ $(m)$ | 2E-5 |
| Cleat normal stiffness $K_n$ $(Pa/m)$ | 100E9 |
| Cleat shear stiffness $K_s$ $(Pa/m)$ | 25E9 |
| Maximum cleat closure ratio | 0.5 |
| Joint Roughness coefficient $JRC$ | 0 |
| Sorption time $\tau$ (days) | 3 |
| Langmuir volume $V_L$ $(m^3/kg)$ | 0.02 |
| Langmuir pressure $P_L$ $(Pa)$ | 1.5E6 |
| Matrix shrinkage coefficient $\beta_\varepsilon$ $(kg/m^3)$ | 0.4 |
| Entry capillary pressure $p_e$ $(Pa)$ | 10000 |
| Cleat size distribution index $\lambda$ | 0.25 |
| Tortuosity coefficient $\eta$ | 1 |
| Initial residual water saturation $S_{r,res_0}$ | 0.1 |
| Residual water saturation exponent, $n_{wr}$ | 0.5 |
| Residual gas saturation | 0.0 |

Table 3: Reservoir and well parameters used in the reference case.

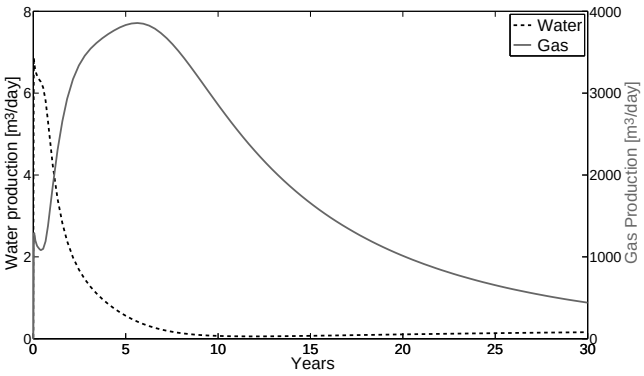


Figure 22: Reference case: water and gas production profiles.

The water and gas production profiles are plotted for 30 years from the start of the production in Figure 22. The peak of water production occurs soon after the beginning of the production. The water production is close to zero from the $10^{\text{th}}$ year but it is never null since the outer boundary is not assumed totally impermeable to water (Equation 94). For gas, relative permeabilities play an important role. While the production of water decreases, the gas production increases. Of course, as the gas tank is a closed volume, it can not indefinitely increases. A peak in the gas production is experienced after the $6^{\text{th}}$ year, at this time, the gas rate is about 3850 standard $m^3/day$. Then, after the peak is observed, the gas production exponentially declines. In Figure 23, it results in a straight line on a semi-log plot of gas rate versus time [8].

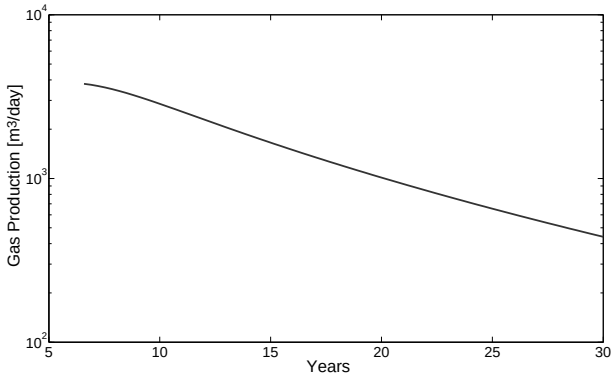


Figure 23: Reference case: gas production profile after peak in a semi-log plot.

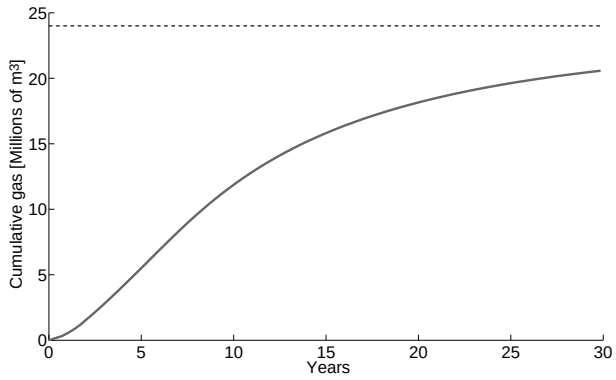


Figure 24: Reference case: cumulative gas.

After 30 years, the cumulative quantity of gas produced is more than 20 millions cubic meters (Figure 24). Knowing the volume of the reservoir and the Langmuir's parameters, the total amount of gas adsorbed at $2MPa$ is 43 millions of cubic meters. As the minimal borehole pressure is $0.5MPa$, it means 19 millions of cubic meters cannot be produced. Thence, 24 millions of cubic meters could be released.

### *7.2. Parametric and couplings analysis*

The proposed model considers both the evolutions of permeability and porosity during the production. The permeability

and porosity evolutions result from a competition between the increase of effective stress due to the reservoir depletion and the desorption strain following the gas production. Figure 25 compares gas production profiles from the synthetic reference simulation with cases where the couplings are limited. One simulation is performed with a constant aperture of the fractures, *i.e.* constant permeability and porosity, a second one where only the permeability is constant and a third one where only the porosity is constant. Figures 26 and 27 show respectively the corresponding evolutions of the porosity and the permeability in the direction perpendicular to the well, plotted at $50cm$ from the well and mid-thickness of the seam. Figure 25 shows permeability and porosity evolutions impact the kinetics of the production. It appears the production peak occurs earlier and higher for cases where the permeability is kept constant. Indeed, when the permeability evolution is allowed, Figure 27 shows the permeability first decreases due to the reservoir depletion and many years are required to recover the initial permeability due to desorption. In fact, the decrease of the permeability following the increase of effective stress occurs directly after the pressure drop while the increase of the permeability due to the matrix shrinkage is not immediate. The peak is also slightly higher when the porosity is not constant. Figure 28 shows the water pressure is decreased faster when the porosity increases, more space being available for the fluids. On the first hand, gas permeability is increased faster thanks to the faster decrease of the water saturation. On the other hand, gas desorption increases with the decrease of the water pressure. These phenomena are responsible for an increase in gas production.

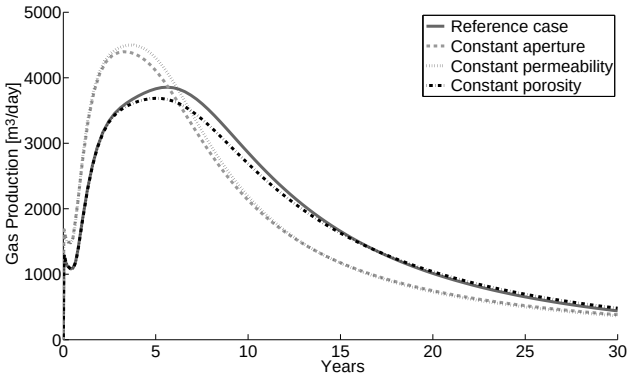


Figure 25: Gas production curves.

Figure 29 shows the radial permeability right next to the well for different sorption time factors. The longer is the sorption time factor, the later the inversion of permeability curve. However, at the time scale of the life of the well, the desorption time has a minor impact on the gas production profile which is controlled by Darcy flow when this characteristic time is about few days [6].

The desorption strain coefficient is a very significant parameter. Obviously, if the desorption strain is neglected ($\beta = 0\ kg/m^3$), the permeability never increases after the decrease due to the depletion. The peak production is therefore lower. Figures 30 and 31 present also an intermediate case.

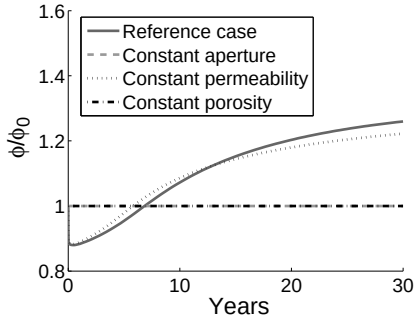


Figure 26: Porosity evolution at $50cm$ from the well.

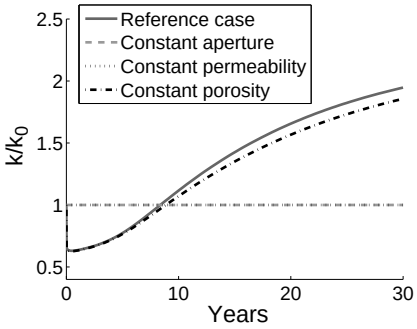


Figure 27: Radial permeability evolution at $50cm$ from the well.

The depletion rate influences also the permeability evolution. Indeed, the pressure drop set in 10 days does not let enough time for desorption strain to counterbalance immediately the increase of effective stress. This time, the pressure well is decreased from 2 to $0.5MPa$ in 5 years. In this case, the dotted permeability evolution in Figure 32 has a less lower minima than the reference case. The gas production peak is delayed but it is slightly higher (Figure 33). It appears also when the pressure drop at the well is less abrupt there is not a brief decrease in the gas production right after the pressure is maintained constant.

Previously, the gas content in the matrix was assumed equal to the maximum capacity, *i.e.* on the Langmuir's isotherm. For the pressure of the reservoir equal to $2MPa$, the maximum adsorbed gas pressure is

$$p_{g,m}^{max} = \frac{RT}{M_g} \cdot \rho_{g,std} \cdot \rho_c \cdot \frac{V_L \cdot p_{res}}{P_L + p_{res}} = 1.897\ MPa \qquad (95)$$

The fact that the adsorbed gas pressure is on the isotherm means the desorption mechanism is activated right after the decrease of the reservoir pressure. Now, let assume only 90% of the maximal capacity is adsorbed in the matrix. Then, the desorption starts from a critical pressure equal to

$$p_{res}^{crit} = \frac{0.9 \cdot p_{g,m}^{max} \cdot P_L}{\left(\frac{RT}{M_g} \cdot \rho_{g,std} \cdot \rho_c \cdot V_L - 0.9 \cdot p_{g,m}^{max}\right)} = 1.588\ MPa \qquad (96)$$

Thence, any gas is desorbed until the pressure of $1.588\ MPa$ is reached in the reservoir. The production peaks therefore later. It is also lower since there is less gas in the reservoir. In fact,

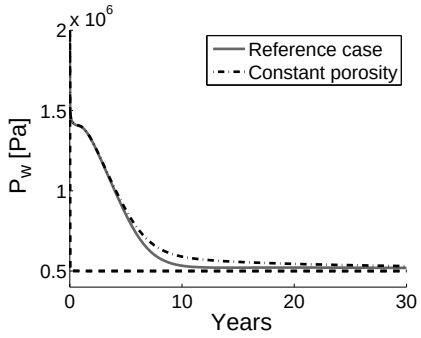


Figure 28: Water pressure evolution at 50*cm* from the well.

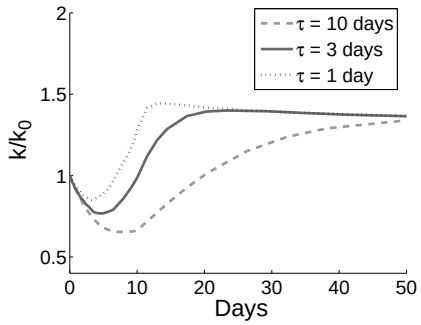


Figure 29: Radial permeability right next to the well.

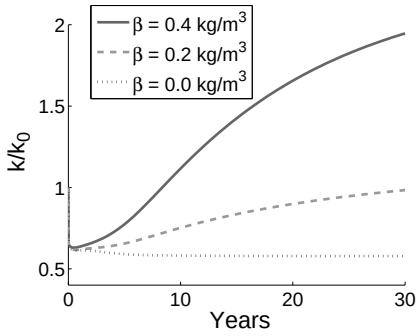


Figure 30: Influence of the desorption strain on the radial permeability at 50*cm* from the well.

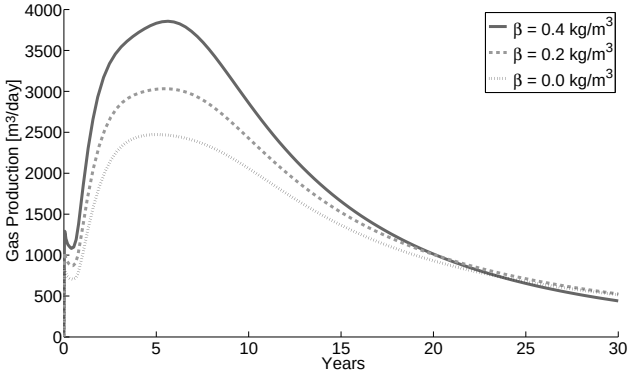


Figure 31: Influence of the desorption strain on the gas production curve.

it is better to drop the pressure from 2*MPa* to 1.588*MPa* as soon as possible. Indeed, whatever the depletion rate chosen, no favourable permeability change can occur during this period. The last production scenario considers a pressure drop from 2*MPa* to 1.588*MPa* in 10 days and then the pressure is decreased to reach 0.5*MPa* after 5 years. This production scenario does not lower the minimal radial permeability and the production peak is earlier.

### *7.3. Horseshoe Canyon case*

In this section, pressure and gas rate data presented by Gerami *et al.* [85] for a well drilled in the Horseshoe Canyon coals from the Western Canadian Sedimentary Basin are used for a history matching exercise in order to test the permeability model. As this well does not produce water, this exercise is simplified since relative permeabilities do not play a role in the production behaviour. Reservoir properties provided by Gerami *et al.* are listed in Table 4. As part of their analysis, they also estimated a total initial gas-in-place of 6.36 millions of standard cubic meters. Other parameters, such as matrix shrinkage coefficient, were not reported.

Given the Langmuir's parameters and the reservoir pressure, the maximal amount of adsorbed gas is 2.14E-03 $m^3/kg$ (Equation 56). Assuming 90% of this maximum capacity is actually stored, there are 2.83 of standard cubic meters of gas per cubic meter of coal. Therefore, the volume of 6.36 millions of standard cubic meters of gas is stored in a reservoir volume of 2.25 millions of cubic meters. Given the thickness of the seam, the radius of the cylindrical reservoir is 282*m*. From the porosity of 0.5%, many combinations of the fracture aperture

| Parameters | Values |
|---|---|
| Initial reservoir pressure ($Pa$) | 1.416E6 |
| Temperature ($K$) | 289 |
| Coal density ($kg/m^3$) | 1468 |
| Seam thickness ($m$) | 8.99 |
| Porosity $\phi_f$ | 0.005 |
| Langmuir volume $V_L$ ($m^3/kg$) | 0.0092 |
| Langmuir pressure $P_L$ ($Pa$) | 4.652E6 |

Table 4: Reservoir parameters for Horseshoe Canyon coals [85].

and the block width may be considered (Equation 34), giving different values of the permeability. It takes part in the calibration process. Reservoir parameters used to calibrate the model are listed in Table 5. The block matrix width and the fracture aperture used in the calibration to meet a porosity of 0.5% are respectively 8*mm* and 0.01333*mm*, it corresponds to a permeability $k = 4.935\text{E-}14\ m^2$.

Figure 34 presents and compares data from Gerami *et al.* [85] with results of the simulation performed with parameters provided in Tables 4 and 5. The pressure at the well is given as input to the model and the production rate is observed as the answer of the model to this loading. Parameters obtained in Table 5 by reverse analysis are one set of parameters which relatively accurately represent the production data. Of course, the solution is non-unique and it can not be asserted the taken values are physically accurate. More experimental data and information

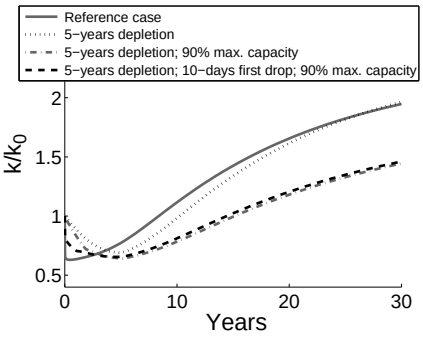


Figure 32: Influence of the depletion rate and gas content on the radial permeability at 50$cm$ from the well.

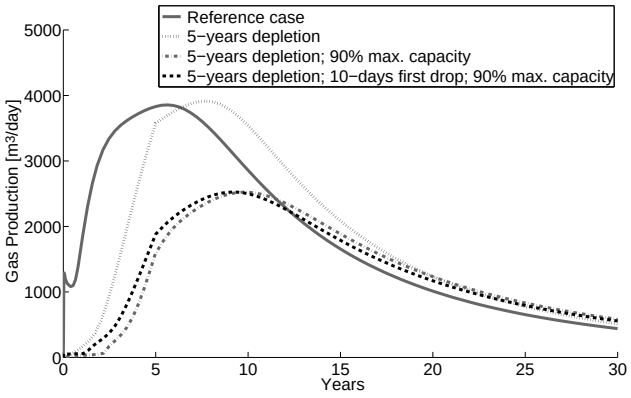


Figure 33: Influence of the depletion rate and gas content on the gas production profile.

| Parameters | Values |
|---|---|
| Reservoir radius ($m$) | 282 |
| Overburden pressure ($Pa$) | 5E6 |
| Matrix Young's modulus $E_m$ ($Pa$) | 5E9 |
| Matrix Poisson's ratio $\nu_m$ | 0.3 |
| Matrix width $w$ ($m$) | 0.008 |
| Cleat aperture $h$ ($m$) | 1.333E-5 |
| Cleat normal stiffness $K_n$ ($Pa/m$) | 100E9 |
| Cleat shear stiffness $K_s$ ($Pa/m$) | 2.5E9 |
| Maximum cleat closure ratio | 0.5 |
| Sorption time $\tau$ (days) | 100 |
| Matrix shrinkage coefficient $\beta_\epsilon$ ($kg/m^3$) | 0.5 |

Table 5: Reservoir parameters used to calibrate the model for the Horseshoe Canyon case.

would be required to ensure this. However, it proves the model is able to represent production data from a real case. Compared to the model presented by Gerami *et al.* [85], gas desorption is not considered instantaneous since the kinetics of diffusion is taken into account thanks to the shape factor. Moreover, compaction is not neglected, the hydro-mechanical couplings are considered to account for the permeability evolution.

An interesting output occurs at around 170 days, whereas the well pressure increases, the gas production decreases and later, when the well pressure rapidly decreases, the gas rate increases. Indeed, the model answers to a variation of the well pressure

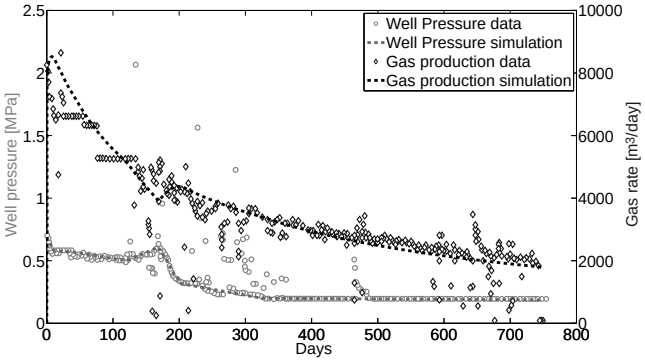


Figure 34: Production history matching. Horseshoe Canyon data from [85].

with an opposite variation in the production. It could not be shown with the synthetic reference case since a simpler loading was carried out.

## 8. Conclusion

This paper presented a hydro-mechanical model for the modeling of coalbed methane production. The main objective of this paper was to formulate a consistent model taking into account the permeability evolution resulting from the reservoir pressure depletion. Indeed, coalbed methane production is a highly coupled problem. It requires to enrich the macroscale with microscale aspects. A novelty is to consider simultaneously a dual-continuum approach for both mechanical and hydraulic behaviours in order to, contrary to many models in the literature, directly link the permeability evolution to the fracture aperture instead of the porosity evolution. A remarkable feature of the model is that it does not consider desorption strain is necessarily fully converted into a fracture opening. Moreover, the model was developed for multiphase flows in the fractures. Beside advective flows in the cleats, the model considers, thanks to shape factors, the influence of the kinetics of diffusion on the mass transfer between the matrix and the fractures. The Langmuir's isotherm is used to evaluate the gas pressure in the matrix. However, it is not usual to also use this isotherm in the mass transfer equation. This hydro-mechanical model was implemented numerically with a finite element method in the Lagamine code. Finally, it was applied to the modeling of the CBM production at the scale of one well. Simulations on a hypothetical reservoir showed it is interesting to not drop the pressure at the well too fast in order to reduce the closure of the fracture due to the increase of effective stress. However, in the case the reservoir does not store the maximal adsorbed gas capacity, it is advisable to apply a first pressure drop until the desorption mechanism is activated. This pressure can be estimated if the adsorbed gas content and the Langmuir's parameters of the coal reservoir are known. The model was also applied to a real production well in the Horseshoe Canyon coals. This dry reservoir presents a different production profile from a water saturated reservoir. However, it allows to simplify the history matching production data exercise since the relative

permeability parameters do not have to be calibrated. This exercise showed the model is also suitable for the modeling of this particular kind of coal reservoir.

## Nomenclature

*Acronyms*

| | | |
|---|---|---|
| *CBM* | Coalbed methane | |
| *JRC* | Joint roughness coefficient | |

*Greek Symbols*

| | | |
|---|---|---|
| $1/\chi_w$ | Water compressibility | $[M^{-1}LT^2]$ |
| $\alpha_\varepsilon$ | Sorption-induced linear strain coefficient | $[-]$ |
| $\beta_\varepsilon$ | Volumetric sorption-induced strain coefficient | $[ML^{-3}]$ |
| $\delta_{ij}$ | Kronecker symbol | $[-]$ |
| $\eta$ | Tortuosity parameter | $[-]$ |
| $\eta_\pi$ | Volume fraction of the phase $\pi$ | $[-]$ |
| $\Gamma$ | External surface of the domain | $[ML^{-1}T^{-2}]$ |
| $\Lambda$ | Tortuosity | $[-]$ |
| $\lambda$ | Cleat size distribution index | $[-]$ |
| $\mu$ | Dynamic viscosity | $[ML^{-1}T^{-1}]$ |
| $\nu_m$ | Poisson's ratio of the matrix | $[-]$ |
| $\nu_{ij}$ | Poisson's ratios of the equivalent medium | $[-]$ |
| $\Omega$ | Control volume | $[L^3]$ |
| $\Omega_\pi$ | Volume of the phase $\pi$ in the control volume | $[L^3]$ |
| $\phi$ | Porosity | $[-]$ |
| $\phi_f$ | Porosity from fractures | $[-]$ |
| $\Psi$ | Shape factor | $[L^{-2}]$ |
| $\rho_c$ | Coal density | $[ML^{-3}]$ |
| $\rho_s$ | Solid density | $[ML^{-3}]$ |
| $\rho_v$ | Water vapour density | $[ML^{-3}]$ |
| $\rho_w$ | Water density | $[ML^{-3}]$ |
| $\rho_{g,Ad}$ | Density of the gas adsorbed on the matrix | $[ML^{-3}]$ |
| $\rho_{g,f}$ | Gas density in the cleats | $[ML^{-3}]$ |
| $\rho^d_{g,f}$ | Density of the dissolved gas in water | $[ML^{-3}]$ |
| $\rho_{g,std}$ | Gas density at standard conditions | $[ML^{-3}]$ |
| $\sigma_{ij}$ | Stress tensor | $[ML^{-1}T^{-2}]$ |
| $\Upsilon$ | Storage term | $[ML^{-3}]$ |
| $\varepsilon_{ij}$ | Strain tensor | $[-]$ |
| $\varphi$ | Flux | $[ML^{-2}T^{-1}]$ |
| $G_{ij}$ | Shear moduli of the equivalent medium | $[ML^{-1}T^{-2}]$ |
| $H_g$ | Henry's coefficient | $[-]$ |
| $\varepsilon_{vs}$ | Volumetric sorption-induced strain | $[-]$ |
| $\varepsilon_{ii_s}$ | Sorption-induced linear strain in the direction $i$ | $[-]$ |

*Roman Symbols*

| | | |
|---|---|---|
| $\bar{t}_i$ | External traction force | $[ML^{-1}T^{-2}]$ |
| $b_{ij}$ | Biot's coefficient tensor | $[-]$ |
| $C$ | Concentration | $[NL^{-3}]$ |
| $C_{ijkl}$ | Stiffness tensor | $[ML^{-1}T^{-2}]$ |
| $D^\alpha_\beta$ | Diffusion coefficient of the species $\alpha$ through $\beta$ | $[L^2T^{-1}]$ |
| $D_{ijkl}$ | Compliance tensor | $[M^{-1}LT^2]$ |
| $E$ | Mass exchange between matrix blocks and fractures | $[MT^{-1}]$ |
| $E_i$ | Young's moduli of the equivalent medium | $[ML^{-1}T^{-2}]$ |
| $E_m$ | Young's modulus of the matrix | $[ML^{-1}T^{-2}]$ |
| $f_{g_i}$ | Internal total flux of gas | $[ML^{-2}T^{-1}]$ |
| $f_{w_i}$ | Internal total flux of water | $[ML^{-2}T^{-1}]$ |
| $h$ | Fracture aperture | $[L]$ |
| $h_b$ | Hydraulic fracture aperture | $[L]$ |
| $K_m$ | Bulk modulus of the matrix blocks | $[ML^{-1}T^{-2}]$ |
| $K_n$ | Normal stiffness of the fracture | $[ML^{-2}T^{-2}]$ |
| $k_{ij}$ | Permeability tensor | $[L^2]$ |
| $k_{rg}$ | Gas relative permeability | $[-]$ |
| $k_{rw}$ | Water relative permeability | $[-]$ |
| $M_g$ | Gas molecular mass | $[MN^{-1}]$ |
| $N$ | Number of sets of fractures | $[-]$ |

| | | |
|---|---|---|
| $n_i$ | Unit vector normal to the boundary | $[-]$ |
| $p_c$ | Capillary pressure | $[ML^{-1}T^{-2}]$ |
| $p_e$ | Entry capillary pressure | $[ML^{-1}T^{-2}]$ |
| $P_L$ | Langmuir pressure | $[ML^{-1}T^{-2}]$ |
| $p_w$ | Water pressure | $[ML^{-1}T^{-2}]$ |
| $p_{g,f}$ | Gas pressure in the fractures | $[ML^{-1}T^{-2}]$ |
| $p_{g,m}$ | Gas pressure in the matrix | $[ML^{-1}T^{-2}]$ |
| $p_{res}$ | Reservoir pressure | $[ML^{-1}T^{-2}]$ |
| $Q$ | Source term | $[ML^{-3}T^{-1}]$ |
| $R$ | Universal gas constant | $[ML^2N^{-1}\theta^{-1}T^{-2}]$ |
| $R_{ij}$ | Rotation matrix | $[-]$ |
| $S_r$ | Saturation degree | $[-]$ |
| $S_r^*$ | Normalized saturation | $[-]$ |
| $S_{r,res}$ | Residual saturation | $[-]$ |
| $T$ | Temperature | $[\theta]$ |
| $t$ | Time | $[T]$ |
| $u_n$ | Normal displacement | $[L]$ |
| $V_L$ | Langmuir volume | $[L^3M^{-1}]$ |
| $V_{g,Ad}$ | Adsorbed volume per unit of mass | $[L^3M^{-1}]$ |
| $w$ | Matrix width | $[L]$ |
| $x$ | Spatial coordinates | $[L]$ |
| $J^g_{g\,i}$ | Diffusive flow of the gas in the gas phase | $[LT^{-1}]$ |
| $J^w_{g\,i}$ | Diffusive flow of water vapour | $[LT^{-1}]$ |
| $J^g_{l\,i}$ | Diffusive flow of the dissolved gas in the liquid phase | $[LT^{-1}]$ |
| $q_{g_i}$ | Gas advective flow | $[LT^{-1}]$ |
| $q_{l_i}$ | Liquid advective flow | $[LT^{-1}]$ |
| $q_g$ | Input gas flux | $[ML^{-2}T^{-1}]$ |
| $q_w$ | Input water flux | $[ML^{-2}T^{-1}]$ |


## Acknowledgements

These researches are supported by the FNRS-FRIA.


## References


[1] R. M. Flores, "Coalbed methane: from hazard to resource," *International Journal of Coal Geology*, vol. 35, no. 1, pp. 3–26, 1998.

[2] J. Ayoub, L. Colson, J. Hinkel, D. Johnston, and J. Levine, "Learning to produce coalbed methane," *Oilfield Review*, vol. 3, no. 1, pp. 27–40, 1991.

[3] I. Palmer, "Coalbed methane completions: a world view," *International Journal of Coal Geology*, vol. 82, no. 3, pp. 184–195, 2010.

[4] T. A. Moore, "Coalbed methane: a review," *International Journal of Coal Geology*, vol. 101, pp. 36–81, 2012.

[5] S. Laubach, R. Marrett, J. Olson, and A. Scott, "Characteristics and origins of coal cleat: a review," *International Journal of Coal Geology*, vol. 35, no. 1, pp. 175–207, 1998.

[6] J. Seidle, *Fundamentals of coalbed methane reservoir engineering*. PennWell Books, 2011.

[7] A. Al-Jubori, S. Johnston, C. Boyer, S. W. Lambert, O. A. Bustos, J. C. Pashin, and A. Wray, "Coalbed methane: clean energy for the world," *Oilfield Review*, vol. 21, no. 2, pp. 4–13, 2009.

[8] A. Salmachi and Z. Yarmohammadtooski, "Production data analysis of coalbed methane wells to estimate the time required to reach to peak of gas production," *International Journal of Coal Geology*, vol. 141, pp. 33–41, 2015.

[9] A. Gilman and R. Beckie, "Flow of coal-bed methane to a gallery," *Transport in porous media*, vol. 41, no. 1, pp. 1–16, 2000.

[10] M. Lu and L. D. Connell, "A dual-porosity model for gas reservoir flow incorporating adsorption behaviourpart i. theoretical development and asymptotic analyses," *Transport in porous media*, vol. 68, no. 2, pp. 153–173, 2007.

[11] I. Gray *et al.*, "Reservoir engineering in coal seams: Part 1-the physical process of gas storage and movement in coal seams," *SPE Reservoir Engineering*, vol. 2, no. 01, pp. 28–34, 1987.

[12] M. Mazzotti, R. Pini, and G. Storti, "Enhanced coalbed methane recovery," *The Journal of Supercritical Fluids*, vol. 47, no. 3, pp. 619–627, 2009.

[13] S. Mazumder, F. Vermolen, J. Bruining, *et al.*, "Analysis of a model for anomalous-diffusion behavior of $CO_2$ in the macromolecular-network structure of coal," *SPE Journal*, vol. 16, no. 04, pp. 856–863, 2011.

[14] J. Q. Shi, S. Durucan, and E. Syahrial, "Reservoir depletion induced changes in coalbed permeability and implications for enhanced cbm recovery using co injection," *Geologica Belgica*, 2006.

[15] X. R. Wei, G. X. Wang, P. Massarotto, S. D. Golding, V. Rudolph, *et al.*, "A review on recent advances in the numerical simulation for coalbed-methane-recovery process," *SPE Reservoir Evaluation & Engineering*, vol. 10, no. 06, pp. 657–666, 2007.

[16] R. Charlier, *Approche unifiée de quelques problèmes non linéaires de mécanique des milieux continus par la méthode des éléments finis (grandes déformations des métaux et des sols, contact unilatéral de solides, conduction thermique et écoulements en milieu poreux)*. PhD thesis, Université de Liège, 1987.

[17] A.-M. Habraken, *Contribution à la modélisation du formage des métaux par la méthode des éléments finis*. PhD thesis, Universté de Liège, 1989.

[18] O. Coussy, *Mechanics of porous continua*. Wiley, 1995.

[19] S. Panday and M. Y. Corapcioglu, "Reservoir transport equations by compositional approach," *Transport in Porous Media*, vol. 4, no. 4, pp. 369–393, 1989.

[20] S. Olivella, J. Carrera, A. Gens, and E. Alonso, "Nonisothermal multiphase flow of brine and gas through saline media," *Transport in porous media*, vol. 15, no. 3, pp. 271–293, 1994.

[21] F. Collin, *Couplages thermo-hydro-mécaniques dans les sols et les roches tendres partiellement saturés*. PhD thesis, Université de Liège, Belgique, 2003.

[22] L. E. Malvern, *Introduction to the Mechanics of a Continuous Medium*. No. Monograph, 1969.

[23] G. Barenblatt, I. P. Zheltov, and I. Kochina, "Basic concepts in the theory of seepage of homogeneous liquids in fissured rocks [strata]," *Journal of applied mathematics and mechanics*, vol. 24, no. 5, pp. 1286–1303, 1960.

[24] P. Newman, "Plastic flow in coal," *British Journal of Applied Physics*, vol. 6, no. 10, p. 348, 1955.

[25] J. R. Levine, "Model study of the influence of matrix shrinkage on absolute permeability of coal bed reservoirs," *Geological Society, London, Special Publications*, vol. 109, no. 1, pp. 197–212, 1996.

[26] N. Berkowitz, *An introduction to coal technology*. Elsevier, 1979.

[27] L. H. Reiss, *The reservoir engineering aspects of fractured formations*, vol. 3. Editions Technip, 1980.

[28] T. D. van Golf-Racht, *Fundamentals of fractured reservoir engineering*, vol. 12. Elsevier, 1982.

[29] H.-H. Liu, J. Rutqvist, and J. G. Berryman, "On the relationship between stress and elastic strain for porous and fractured rock," *International Journal of Rock Mechanics and Mining Sciences*, vol. 46, no. 2, pp. 289–296, 2009.

[30] A. Szwilski, "Determination of the anisotropic elastic moduli of coal," in *International Journal of Rock Mechanics and Mining Sciences & Geomechanics Abstracts*, vol. 21, pp. 3–12, Elsevier, 1984.

[31] R. E. Goodman, *Methods of geological engineering in discontinuous rocks*. 1976.

[32] A. Fossum, "Effective elastic properties for a randomly jointed rock mass," in *International Journal of Rock Mechanics and Mining Sciences & Geomechanics Abstracts*, vol. 22, pp. 467–470, Pergamon, 1985.

[33] S. Bandis, A. Lumsden, and N. Barton, "Fundamentals of rock joint deformation," in *International Journal of Rock Mechanics and Mining Sciences & Geomechanics Abstracts*, vol. 20, pp. 249–268, Elsevier, 1983.

[34] S. Lekhnitskii, *Theory of Elasticity of an Anisotropic Elastic Body*, vol. 525. San Francisco: Holden-Day, 1963.

[35] J. Graham and G. Houlsby, "Anisotropic elasticity of a natural clay," *Géotechnique*, vol. 33, no. 2, pp. 165–180, 1983.

[36] B. Amadei and R. Goodman, "A 3-d constitutive relation for fractured rock masses," *Studies in applied mechanics, part B*, vol. 5, pp. 249–268, 1981.

[37] F. Gu and R. Chalaturnyk, "Permeability and porosity models considering anisotropy and discontinuity of coalbeds and application in coupled simulation," *Journal of Petroleum Science and Engineering*, vol. 74, no. 3, pp. 113–131, 2010.

[38] S. Harpalani and A. Schraufnagel, "Measurement of parameters impacting methane recovery from coal seams," *International Journal of Mining and Geological Engineering*, vol. 8, no. 4, pp. 369–384, 1990.

[39] A. Mitra, S. Harpalani, and S. Liu, "Laboratory measurement and modeling of coal permeability with continued methane production: Part 1–laboratory results," *Fuel*, vol. 94, pp. 110–116, 2012.

[40] H. Darcy, *Les fontaines publiques de la ville de Dijon*. Librairie des Corps Impriaux des Ponts et Chausses et des Mines, 1856.

[41] J. Bear, C.-F. Tsang, and G. De Marsily, *Flow and contaminant transport in fractured rock*. Academic Press, 1993.

[42] S. P. Neuman, "Theoretical derivation of darcy's law," *Acta Mechanica*, vol. 25, no. 3-4, pp. 153–170, 1977.

[43] N. Barton, S. Bandis, and K. Bakhtar, "Strength, deformation and conductivity coupling of rock joints," in *International Journal of Rock Mechanics and Mining Sciences & Geomechanics Abstracts*, vol. 22, pp. 121–140, Elsevier, 1985.

[44] N. Barton and V. Choubey, "The shear strength of rock joints in theory and practice," *Rock mechanics*, vol. 10, no. 1-2, pp. 1–54, 1977.

[45] Z. Pan and L. D. Connell, "Modelling permeability for coal reservoirs: a review of analytical models and testing data," *International Journal of Coal Geology*, vol. 92, pp. 1–44, 2012.

[46] I. Palmer, J. Mansoori, *et al.*, "How permeability depends on stress and pore pressure in coalbeds: a new model," in *SPE Annual Technical Conference and Exhibition*, Society of Petroleum Engineers, 1996.

[47] X. Cui and R. M. Bustin, "Volumetric strain associated with methane desorption and its impact on coalbed gas production from deep coal seams," *Aapg Bulletin*, vol. 89, no. 9, pp. 1181–1202, 2005.

[48] F. O. Jones Jr *et al.*, "A laboratory study of the effects of confining pressure on fracture flow and storage capacity in carbonate rocks," *Journal of Petroleum Technology*, vol. 27, no. 01, pp. 21–27, 1975.

[49] W. H. Somerton, I. Soylemezoglu, and R. Dudley, "Effect of stress on permeability of coal," in *International journal of rock mechanics and mining sciences & geomechanics abstracts*, vol. 12, pp. 129–145, Elsevier, 1975.

[50] A. T. Corey, "The interrelation between gas and oil relative permeabilities," *Producers monthly*, vol. 19, no. 1, pp. 38–41, 1954.

[51] D. Chen, Z. Pan, J. Liu, and L. D. Connell, "An improved relative permeability model for coal reservoirs," *International Journal of Coal Geology*, vol. 109, pp. 45–57, 2013.

[52] R. H. Brooks and A. T. Corey, "Hydraulic properties of porous media and their relation to drainage design," *Transactions of the ASAE*, vol. 7, no. 1, pp. 26–0028, 1964.

[53] L. Kewen *et al.*, "Theoretical development of the brooks-corey capillary pressure model from fractal modeling of porous media," in *SPE/DOE Symposium on Improved Oil Recovery*, Society of Petroleum Engineers, 2004.

[54] B. B. Mandelbrot and R. Pignoni, "The fractal geometry of nature," 1983.

[55] A. Fick, "Ueber diffusion," *Annalen der Physik*, vol. 170, no. 1, pp. 59–86, 1855.

[56] E. A. Mason and A. Malinauskas, *Gas transport in porous media: the dusty-gas model*, vol. 17. Elsevier Science Ltd, 1983.

[57] F. Collin, X.-L. Li, J.-P. Radu, and R. Charlier, "Thermo-hydro-mechanical coupling in clay barriers," *Engineering Geology*, vol. 64, no. 2, pp. 179–193, 2002.

[58] R. Sander, "Compilation of henry's law constants (version 4.0) for water as solvent.," *Atmospheric Chemistry & Physics*, vol. 15, no. 8, 2015.

[59] I. Langmuir, "The adsorption of gases on plane surfaces of glass, mica and platinum.," *Journal of the American Chemical society*, vol. 40, no. 9, pp. 1361–1403, 1918.

[60] S. Brunauer, P. H. Emmett, and E. Teller, "Adsorption of gases in multimolecular layers," *Journal of the American chemical society*, vol. 60, no. 2, pp. 309–319, 1938.

[61] P. L. Coppens, *Synthèse des propriétés chimiques et physiques des houilles*. Institut National de l'Industrie Charbonnière, 1967.

[62] J. Warren, P. J. Root, *et al.*, "The behavior of naturally fractured reservoirs," *Society of Petroleum Engineers Journal*, vol. 3, no. 03, pp. 245–255, 1963.

[63] H. Kazemi, L. Merrill Jr, K. Porterfield, P. Zeman, *et al.*, "Numerical simulation of water-oil flow in naturally fractured reservoirs," *Society of Petroleum Engineers Journal*, vol. 16, no. 06, pp. 317–326, 1976.

[64] C. Mora, R. Wattenbarger, *et al.*, "Analysis and verification of dual porosity and cbm shape factors," *Journal of Canadian Petroleum Technology*, vol. 48, no. 02, pp. 17–21, 2009.

[65] Y. Ueda, S. Murata, Y. Watanabe, K. Funatsu, *et al.*, "Investigation of the shape factor used in the dual-porosity reservoir simulator," in *SPE Asia-Pacific Conference*, Society of Petroleum Engineers, 1989.

[66] K. H. Coats *et al.*, "Implicit compositional simulation of single-porosity and dual-porosity reservoirs," in *SPE Symposium on Reservoir Simulation*, Society of Petroleum Engineers, 1989.

[67] M.-M. Chang, "Deriving the shape factor of a fractured rock matrix," tech. rep., National Inst. for Petroleum and Energy Research, Bartlesville, OK (United States), 1993.

[68] R. W. Zimmerman, G. Chen, T. Hadgu, and G. S. Bodvarsson, "A numerical dual-porosity model with semianalytical treatment of fracture/matrix flow," *Water resources research*, vol. 29, no. 7, pp. 2127–2137, 1993.

[69] M. Quintard and S. Whitaker, "Transport in chemically and mechanically heterogeneous porous media. ii: Comparison with numerical experiments for slightly compressible single-phase flow," *Advances in water resources*, vol. 19, no. 1, pp. 49–60, 1996.

[70] K. Lim and K. Aziz, "Matrix-fracture transfer shape factors for dual-porosity simulators," *Journal of Petroleum Science and Engineering*, vol. 13, no. 3, pp. 169–178, 1995.

[71] J. Crank, *The mathematics of diffusion*. Oxford university press, 1979.

[72] M. Nuth and L. Laloui, "Effective stress concept in unsaturated soils: clarification and validation of a unified framework," *International journal for numerical and analytical methods in Geomechanics*, vol. 32, no. 7, pp. 771–801, 2008.

[73] K. v. Terzaghi, "The shearing resistance of saturated soils and the angle between the planes of shear," in *Proceedings of the 1st international conference on soil mechanics and foundation engineering*, vol. 1, pp. 54–56, Harvard University Press Cambridge, MA, 1936.

[74] M. A. Biot, "General theory of three-dimensional consolidation," *Journal of applied physics*, vol. 12, no. 2, pp. 155–164, 1941.

[75] A. Bishop, "The effective stress principle," *Teknisk Ukeblad*, vol. 39, pp. 859–863, 1959.

[76] K. Tuncay and M. Y. Corapcioglu, "Effective stress principle for saturated fractured porous media," *Water Resources Research*, vol. 31, no. 12, pp. 3103–3106, 1995.

[77] B. Schrefler, *The finite element method in soil consolidation*. PhD thesis, University College of Swansea, 1984.

[78] C. Ö. Karacan, "Heterogeneous sorption and swelling in a confined and stressed coal during co2 injection," *Energy & Fuels*, vol. 17, no. 6,

pp. 1595–1608, 2003.
[79] G. Ceglarska-Stefaríska, "Effect of gas pressure in methane induced swelling on the porous structure of coals," *Studies in Surface Science and Catalysis*, vol. 87, pp. 671–677, 1994.
[80] J. S. George and M. Barakat, "The change in effective stress associated with shrinkage from gas desorption in coal," *International Journal of Coal Geology*, vol. 45, no. 2, pp. 105–113, 2001.
[81] S. Ottiger, R. Pini, G. Storti, and M. Mazzotti, "Competitive adsorption equilibria of $CO_2$ and $CH_4$ on a dry coal," *Adsorption*, vol. 14, no. 4-5, pp. 539–556, 2008.
[82] S. Day, R. Fry, and R. Sakurovs, "Swelling of australian coals in supercritical co 2," *International Journal of Coal Geology*, vol. 74, no. 1, pp. 41–52, 2008.
[83] O. C. Zienkiewicz and R. L. Taylor, *The finite element method: solid mechanics*, vol. 2. Butterworth-heinemann, 2000.
[84] D. W. Peaceman *et al.*, "Interpretation of well-block pressures in numerical reservoir simulation (includes associated paper 6988)," *Society of Petroleum Engineers Journal*, vol. 18, no. 03, pp. 183–194, 1978.
[85] S. Gerami, M. P. Darvish, K. Morad, L. Mattar, *et al.*, "Type curves for dry cbm reservoirs with equilibrium desorption," in *Canadian International Petroleum Conference*, Petroleum Society of Canada, 2007.